



OPEN Maximum admittance method for cerebrovascular outlet boundary conditions and importance of stenosis severity as a dominant factor on hemodynamics

Jae Hyun Choi¹, Myeonggi Cha², Seong Min Shin², Jihun Kim¹, Hyug-Gi Kim³, Bum Joon Kim⁴ & HangJin Jo^{1,2}✉

In this study, we propose the maximum admittance method based on an analytical solution of two-element Windkessel model to generate pressure waveforms for imposing outlet boundary conditions in blood flow simulations in the absence of in vivo pressure data. The lumped parameters of the Windkessel model, which were not calibrated from the in vivo pressure, were determined to maximize peripheral admittance. By applying the pressure waveforms at outlet boundaries, hemodynamic characteristics of human cerebrovascular networks, including stenotic middle cerebral arteries (MCAs), were investigated through transient flow simulations. Two age-related flow waveforms, in addition to three different blood viscosities, were applied across each severity case (total 24 simulation cases). The age-related flow waveforms introduced normalized relative residence time disparities exceeding 30% in post-stenosis regions with over 50% severity. Additionally, stenosis exceeding 50% severity redirected more blood flow toward anterior cerebral artery, leading to MCA ischemia at 88% severity. The maximum pressure gradient on the stenotic walls and fractional pressure ratio exhibited changes below 9% and 3%, respectively, despite a 54.5% increase in viscosity. The stenosis severity was a dominant physiological factor, suggesting 50% severity as a critical transition point in cerebral hemodynamics. This threshold can help in quickly identifying risky locations.

Keywords Maximum admittance method, Boundary condition, Hemodynamics, Stenosis severity, Flow waveform, Blood viscosity

Stroke is a significant health risk in modern society, particularly due to its increasing prevalence among the elderly¹. Intracranial atherosclerosis is a common subtype of ischemic stroke in large arteries². The atherosclerosis originates from endothelial damage, which initiates the permeation of low-density lipoprotein (LDL) cholesterol particles through the subendothelial region³. Following the formation of atherosclerotic lesion, it expands and forms arterial stenosis that results in cerebrovascular diseases through occlusion³.

The development of atherosclerosis is closely related to the flow-induced mechanical forces exerted on blood vessels⁴. Wall shear stress (WSS) and plaque structural stress are considered as key hemodynamic contributors to atherosclerosis development⁵. Low-level WSS zones (e.g., downstream of stenosis) promote molecular adhesion to form atherosclerosis, whereas high-level plaque structural stress zones (e.g., upstream of stenosis) are prone to plaque rupture and subsequent thrombosis formation⁵.

The pathogenesis of ischemic stroke in the middle cerebral artery (MCA) is believed to be affected by the occlusion site^{6,7}. Proximal occlusions at the M1 segment are predominantly associated with atherosclerosis, whereas distal occlusions at the M2 bifurcation are associated with cardioembolism⁶. The combined occurrence of plaque rupture with thrombosis is frequently observed in proximal occlusion cases, whereas artery-to-artery

¹Department of Mechanical Engineering, POSTECH, Pohang, Republic of Korea. ²Division of Advanced Nuclear Engineering, POSTECH, Pohang, Republic of Korea. ³Department of Radiology, Kyung Hee University Hospital, Kyung Hee University College of Medicine, Seoul, Republic of Korea. ⁴Department of Neurology, Asan Medical Center, Seoul, Republic of Korea. ✉email: jhj04@postech.ac.kr

embolism is typically observed in patients with distal occlusions⁷. Despite these associations, hemodynamic analyses utilizing fluid mechanics are yet to be reported.

The investigation of flow physics with the progression of stenosis under varied physiological conditions enhances the understanding of ischemic stroke mechanisms. Age-related blood flow waveforms constitute one such factor. The elderly exhibit a pronounced secondary peak in volumetric flow rate in the internal carotid artery (ICA) during the systolic phase when compared to younger adults⁸. Combining the increased arterial stiffness, the flow waveform for the elderly results in significantly lowered cycle-averaged (or time-averaged) WSS⁹. Moreover, the oscillatory shear index (OSI) was increased by over 30% at the ICA aneurysm wall when compared to that of young adults¹⁰.

Additionally, high hematocrit levels were associated with increased ischemic stroke incidence¹¹. However, highly viscous blood inhibits LDL transport to intima layer due to increased flow resistance across endothelium layer¹². Although previous studies reported the impact of hematocrit or viscosity levels on the vascular disease, limited research has been conducted on the critical differences in the physiological factors influencing stenosis progression.

A quantitative evaluation of blood supply obstruction due to stenosis can be achieved through the fractional flow reserve (FFR)¹³ or fractional pressure ratio (FPR)¹⁴. The former is extensively utilized to assess the vessel occlusion severity, particularly in coronary arteries¹⁵. However, FFR measurement in cerebrovascular networks is constrained by its invasive nature, requiring pressure wire insertion into vessels, which presents a risk of thrombosis and potential emergencies in cerebral arteries. In contrast, the computational fluid dynamics (CFD) approach provides a noninvasive method for assessing hemodynamic indices related to vessel occlusion (FFR or FPR)^{16,17}. In addition to noninvasiveness, CFD provides a detailed resolution of hemodynamics across both the spatial and temporal dimensions.

Nonetheless, achieving an accurate diagnosis of hemodynamics using CFD requires precise boundary conditions¹⁸. However, such determination of exact boundary conditions on patient-specific arterial networks generally represents a challenge. Hence, alternatives such as Murray's law¹⁹ and minimum energy loss (MEL) principle²⁰ have been applied to computational hemodynamics. For the selection of two-element Windkessel (WK2) model parameters, controlling scaling factors of resistance and compliance has also been proposed²¹. However, to apply Murray's law, the given diameters captured from actual human cerebrovascular networks should match a basic requirement of Murray's law ($d_{parent}^3 = \sum d_{daughter}^3$). If the diameter correlation between parent and daughter vessels is not satisfied, implementing Murray's law is physically nonsense because it violates mass conservation. Therefore, Murray's law has limits regarding applications to real cerebrovascular networks which have diverse diameter correlations between parent and daughter vessels. Moreover, the MEL principle requires multiple CFD simulations to ascertain optimal flow division ratios at arterial bifurcations, potentially increasing the computational costs when employing a fine grid in the CFD domain. Likewise, the methodology proposed in²¹ may require a long simulation time for convergence, as it numerically solves the governing equations of the WK2 model for the outlet boundary conditions. In response, an analytical solution of the WK2 model was derived in this study to directly apply pressure boundary conditions at arterial outlets. To handle cases involving unavailable in vivo pressure data, the lumped parameters were determined to maximize peripheral admittance of the arterial network through a zero-dimensional (0-D) approach (WK2-MAM elaborated in Section "Outlet: pressure waveform derived from maximum admittance method based on two-element Windkessel model (WK2-MAM)").

With reference to the available literature, extensive research was conducted on cerebrovascular hemodynamics concerning aneurysms^{22–24}; however, more investigations should be conducted on stenotic MCAs to comprehend the ischemic stroke hemodynamics. Therefore, the aim of this study was to investigate the hemodynamic characteristics of human cerebrovascular networks encompassing diverse physiological factors. To identify crucial factors for the stroke mechanism, this investigation selected four MCA stenosis severities, two age-related flow waveforms, and three hematocrit levels encompassing low- to high-viscosity conditions as the physiological factors for the cerebrovascular hemodynamics study (total 24 simulation cases).

Methods

Geometry and computational domain

Figure 1 depicts the transformation of raw vessel images into three-dimensional (3-D) arterial networks for CFD analysis. The cerebrovascular networks of an ischemic stroke patient (62-year-old female with hyperlipidemia) were imaged using magnetic resonance angiography (MRA) at Kyung Hee University Hospital, revealing focal stenosis with a plaque in the proximal M1 segment of the left MCA. This study was approved by the Institutional Review Board of the Kyung Hee University Hospital (no. 2009–12–301), which waived the requirement for informed consent due to retrospective nature of study and minimal risk of data collection to patients. All methods of this study were performed following the relevant guidelines and regulations.

The MRA images (Digital Imaging and Communications in Medicine) were imported into the open-source software 3D Slicer (release 5.2.1) to reconstruct the 3-D arterial models with surface smoothing. A region of interest (ROI), including the stenotic portion of the left MCA, was selected. The ROI consists of ICA, anterior cerebral artery (ACA), and MCA (Fig. 1). The reconstructed cerebrovascular networks within this ROI were then exported as stereolithography (STL) files, which were subsequently imported into ANSYS SpaceClaim for ROI volume acquisition to facilitate mesh generation.

Figure 2 depicts the computational domains ranging from healthy to severely stenotic MCAs. To analyze the hemodynamics in comparison with the MCA stenosis progression, the stenosis within the left MCA (Fig. 1) was manually adjusted using the blending feature in SpaceClaim. Because the cross-sectional planes of the patient-specific cerebral arteries are not completely circular, the stenosis severities were assessed based on the hydraulic diameters of the lumens, as shown in Fig. 2b.

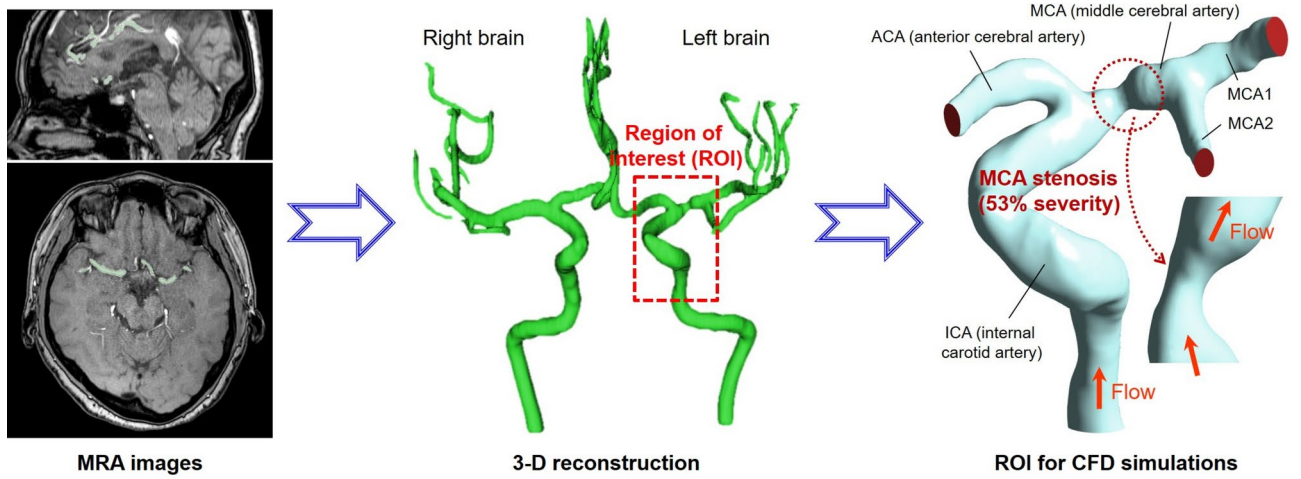


Fig. 1. Reconstruction process of patient-specific cerebrovascular networks for computational fluid dynamics (CFD) simulations.

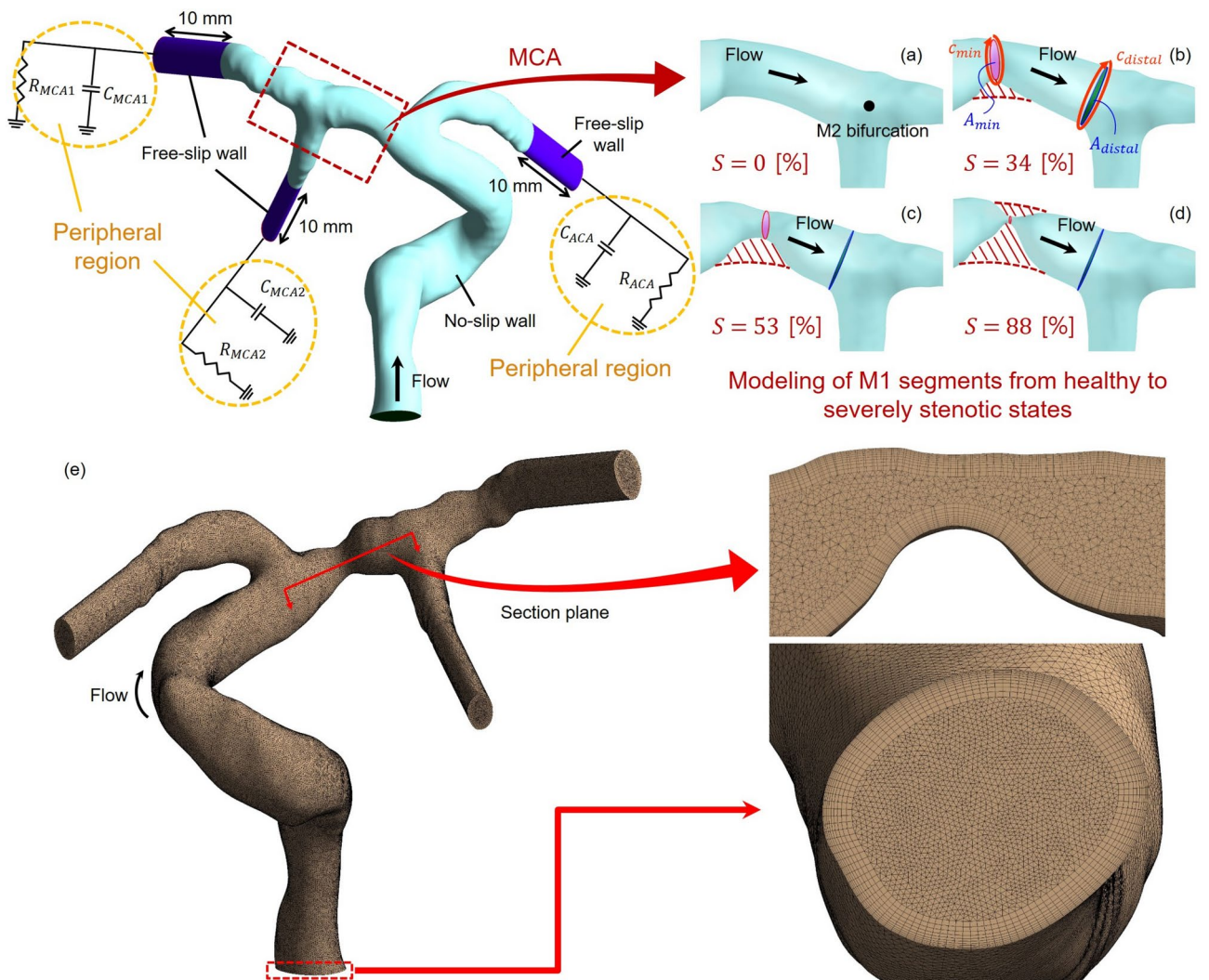


Fig. 2. Computational domains: (a) healthy, (b) normal-mildly stenotic, (c) moderately stenotic, (d) severely stenotic MCAs, and (e) representative example of mesh configuration.

$$S = \left(1 - \frac{d_{h,min}}{d_{h,distal}} \right) \times 100 = \left[1 - \left(\frac{4A}{c} \right)_{min} / \left(\frac{4A}{c} \right)_{distal} \right] \times 100. \quad (1)$$

Adhering to the stenosis classification criteria in²⁵, severities of 34%, 53%, and 88% were classified as normal-mild (Fig. 2b), moderate (Fig. 2c), and severe (Fig. 2d) stenoses, respectively. The MCA with 53% severity, directly reconstructed from the MRA data, along with its grid system, is depicted as a representative example in Fig. 2e.

The computational domains for the cerebrovascular networks were extended by 10 mm at the outlets (Fig. 2) to ensure numerical stability of outflows during CFD simulation procedures. These extensions were determined through preliminary simulations, which did not affect the hemodynamics within the ROI. The walls of these extended domains were designated as free-slip to eliminate frictional losses, considering these extensions as virtual domains aimed at enhancing the convergence of numerical solutions. Further details on the boundary conditions are presented in Section “Treatment of boundary conditions”.

Working fluid and hemodynamic indices

The blood density was set to 1050 kg/m³, assuming blood to be an incompressible fluid. As previously reported²⁶, considering the blood as a Newtonian fluid is suitable for arterial network flow simulations. This is because the disruption of rouleaux formations by shear forces is rapid compared to the aggregation rate of red blood cells, rendering the shear-thinning effect negligible. Similar results have been reported for arterial-scale blood flow simulations²⁷. Consequently, the dynamic viscosity of the blood was calculated using the infinite shear rate equation provided in²⁸, which establishes viscosity values based on the hematocrit levels. Three hematocrit values (0.3, 0.39, and 0.45) were selected to assess hemodynamics corresponding to the blood viscosity²⁸:

$$\mu_{\infty} = 0.005 \left(0.2114 + 0.9067\alpha + 1.9879\alpha^2 \right). \quad (2)$$

Finally, the blood viscosities were determined to be 3.3 mPa·s (low viscosity, $\alpha=0.3$), 4.3 mPa·s (medium viscosity, $\alpha=0.39$), and 5.1 mPa·s (high viscosity, $\alpha=0.45$).

Among the various hemodynamic indices, cycle-averaged WSS, relative residence time (RRT)²⁹, and endothelial cell activation potential (ECAP)³⁰ are well correlated with atherosclerotic disease^{31,32}. This study utilized the RRT as an indicator of low and oscillatory shear zones, normalized to a reference RRT derived theoretically from the Hagen–Poiseuille equation at the ICA inlet (NRRT). Low-level wall shear potentially promotes intimal thickening in the early stages³³, and oscillatory shear may contribute to plaque vulnerability³⁴. Additionally, we utilized the ECAP to simultaneously identify the changes in the WSS and OSI based on the stenosis severity. High-level ECAP corresponds to low cycle-averaged WSS and high OSI at a specific location, which indicates the thrombogenic susceptibility of the vessel wall³⁰. Similar to NRRT, we utilized the theoretical WSS magnitude calculated using the Hagen–Poiseuille equation at the ICA inlet to normalize the cycle-averaged WSS on the vascular walls. The NRRT and ECAP values were computed using MATLAB (version R2020b) following the extraction of WSS vector components from the CFD-Post. The hemodynamic indices examined in this study are summarized in Table 1, with the ICA inlet serving as the reference plane for FPR assessments.

Mesh, CFD solver, and numerical schemes

The cerebrovascular networks were discretized using tetrahedral and prism meshes created with the ANSYS Mesh software. To accurately resolve the boundary layer, up to 10 inflation layers were generated at the arterial walls, maintaining a first layer offset of 15 μm and an expansion ratio of 1.2. The blood flow simulations were executed in ANSYS CFX (version 2020 R1). The preliminary calculations performed to ascertain the dependency on the time step size resulted in the selection of time marching sizes ($= T/20000$) by evaluating a root mean square (RMS) Courant number below 0.45 throughout the cycle. The high-resolution and second-order backward Euler methods were used for the advection and temporal schemes, respectively. The convergence criterion of the numerical solution residuals was established at $\text{RMS } 10^{-6}$. The simulations spanned three cardiac cycles to affirm the periodicity of the pulsatile flow, with 100 result files sampled at equidistant time intervals ($= T/100$) for

| Hemodynamic index | Definition |
|--|---|
| WSS vector ³⁵ | $\boldsymbol{\tau} = 2\mu_{\infty} [D\mathbf{n}_u - ((D\mathbf{n}_u) \cdot \mathbf{n}_u) \mathbf{n}_u]$ where $D = 0.5 [\nabla \mathbf{u} + (\nabla \mathbf{u})^T]$ and \mathbf{n}_u is outward unit normal vector of tangential plane to the vessel wall |
| Cycle-averaged magnitude of WSS vector | $\ \overline{\boldsymbol{\tau}}\ = \frac{1}{T} \int_0^T \ \boldsymbol{\tau}\ dt$ |
| OSI ³⁶ | $\text{OSI} = \frac{1}{2} \left(1 - \frac{\int_0^T \ \boldsymbol{\tau}\ dt}{\int_0^T \ \boldsymbol{\tau}\ dt} \right)$ |
| RRT ²⁹ | $\text{RRT} \sim \left[(1 - 2 \times \text{OSI}) \times \ \overline{\boldsymbol{\tau}}\ \right]^{-1}$ |
| NRRT | $\text{NRRT} = \text{RRT} / \text{RRT}_{H-P}$ where $\text{RRT}_{H-P} \sim d_{h,in} / (8\mu_{\infty} \ \mathbf{u}\ _{in,AA})$, hydraulic diameter $d_{h,in} = 4A_{in}/c_{in}$, and $\ \mathbf{u}\ _{in,AA} = \overline{Q}_{ICA}/A_{in}$ |
| ECAP ³⁰ | $\text{ECAP} = \text{OSI} / (\ \overline{\boldsymbol{\tau}}\ / \ \overline{\boldsymbol{\tau}}\ _{H-P})$ where $\ \overline{\boldsymbol{\tau}}\ _{H-P} = 8\mu_{\infty} \ \mathbf{u}\ _{in,AA} / d_{h,in}$ |
| FPR | $\text{FPR} = \overline{P} / \overline{P}_{in,AA} = \left(\frac{1}{T} \int_0^T P dt \right) / \left(\frac{1}{T} \int_0^T P_{in,AA} dt \right)$ where $P_{in,AA} = \int P_{in} dA / A_{in}$ |

Table 1. Summary of hemodynamic indices.

| | Young adults | | Elderly adults | |
|-------|---------------------------|---------------------------|---------------------------|---------------------------|
| | a_n (m ³ /s) | b_n (m ³ /s) | a_n (m ³ /s) | b_n (m ³ /s) |
| $n=0$ | 4.594×10^{-6} | – | 4.093×10^{-6} | – |
| $n=1$ | -1.332×10^{-7} | 1.14×10^{-6} | -1.9×10^{-7} | 1.738×10^{-6} |
| $n=2$ | -2.484×10^{-7} | 6.825×10^{-7} | -6.456×10^{-7} | 5.609×10^{-7} |
| $n=3$ | -5.163×10^{-7} | 2.216×10^{-7} | -4.802×10^{-7} | -4.054×10^{-9} |
| $n=4$ | -2.581×10^{-7} | 1.032×10^{-7} | -1.064×10^{-7} | 1.437×10^{-7} |
| $n=5$ | -3.712×10^{-7} | -9.968×10^{-8} | -3.466×10^{-7} | -1.054×10^{-8} |
| $n=6$ | -5.259×10^{-8} | -2.579×10^{-7} | -1.017×10^{-7} | -1.822×10^{-7} |
| $n=7$ | 6.75×10^{-8} | -8.398×10^{-8} | -1.859×10^{-8} | -9.478×10^{-8} |
| $n=8$ | 2.919×10^{-8} | -6.826×10^{-8} | 2.489×10^{-8} | -1.016×10^{-7} |

Table 2. Fourier coefficients of the fitted ICA volumetric flow rates.

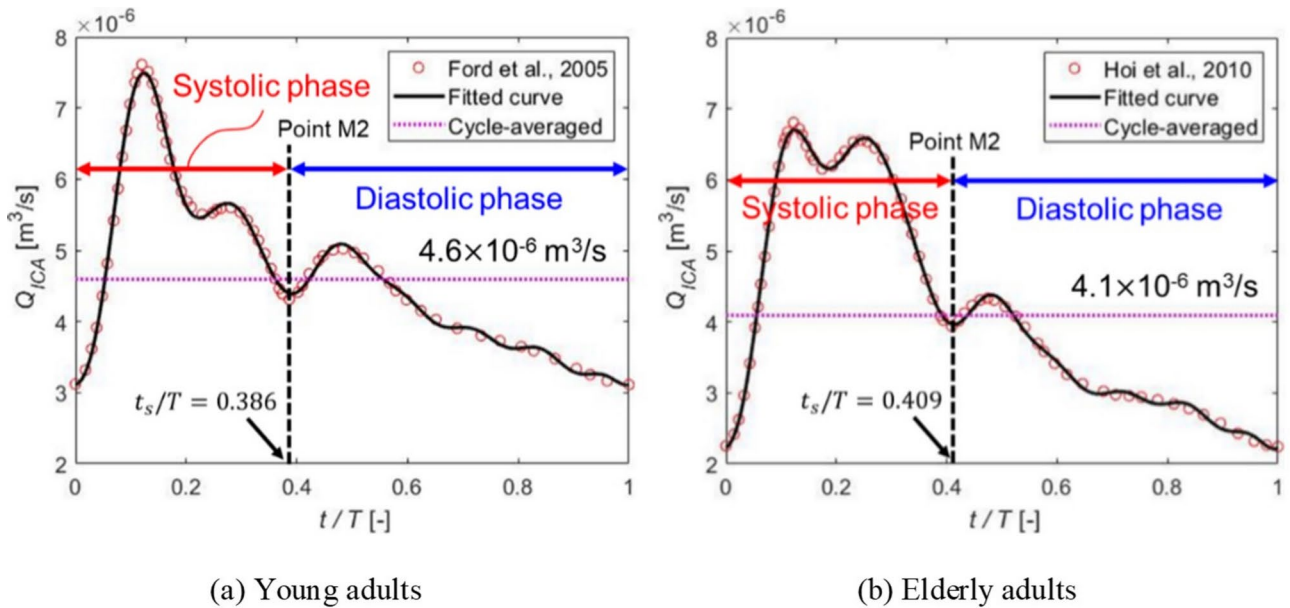


Fig. 3. Blood flow waveforms for inlet boundary conditions^{8,37}.

post-processing of the final cycle data. A laminar flow model was employed for the simulations and is considered to be acceptable despite recirculating flow generation in the post-stenosis zone (Supplementary Fig. S1). For all the cerebrovascular networks, pressure waveforms derived from WK2-MAM (Fig. 6) were set as relative pressure at the outlet boundaries. The outlets were designated as opening boundaries to accommodate potential reverse flow, which was deemed a criterion for identifying the ischemia occurrence. The flow fields were initialized at zero velocity and pressure, assuming rigid arterial walls. The results of grid dependency study were presented in Supplementary Fig. S2. For validation of the CFD solver, simulation setup was listed in Supplementary Table S1 and the results were plotted in Supplementary Fig. S3, validating the accuracy of the CFX solver.

Treatment of boundary conditions

Inlet

Two distinct time-dependent mass flow rate functions were applied to the ICA as the inlet boundary conditions to characterize the influence of the blood flow waveforms by age. The volumetric flow rates for young and elderly adults, derived from³⁷ and⁸, respectively, were modeled using an eight-harmonic Fourier series in MATLAB. The Fourier coefficients are listed in Table 2. The fitted volumetric flow rate functions are presented in Fig. 3, and the inlet mass flow rate functions are determined as follows:

$$\dot{m}_{ICA}(t) = \rho Q_{ICA}(t) = \rho \left[a_0 + \sum_{n=1}^8 \left[a_n \cos\left(\frac{2n\pi t}{T}\right) + b_n \sin\left(\frac{2n\pi t}{T}\right) \right] \right]. \quad (3)$$

As shown in Fig. 3, the systolic phase durations of the young and elderly adults were $t_s/T = 0.386$ and $t_s/T = 0.409$, respectively. These are the feature points denoted as “M2” in the literature^{8,37}. The pulsatile flow periods were 0.883 and 0.949 s for the young and elderly adults, respectively.

Outlet: pressure waveform derived from maximum admittance method based on two-element Windkessel model (WK2-MAM)

In the CFD simulations of arterial systems with multiple outlets, applying zero pressure at all the outlet boundaries is known to yield inaccurate flow divisions between the arterial branches^{38,39}. Consequently, the Windkessel model was utilized to produce pressure waveforms for the outlet boundary condition. This model is a 0-D or lumped parameter method that describes the blood flows based on hydraulic-electrical systems analogy⁴⁰. In this analogy, the blood pressure and flow rate are correlated with voltage and current in an electrical circuit, respectively. The Windkessel models vary in complexity based on the number of elements in the electrical analog circuit, with multiple configurations available⁴¹. The simplest of these models, the WK2 model (Supplementary Fig. S4), includes resistance and compliance to represent flow resistance and vessel elasticity, respectively⁴¹. Despite its lower accuracy compared to those of three- or four-element models^{40,41}, the WK2 model has been successfully employed as the outlet boundary condition in arterial network CFD simulations^{39,42}. However, selecting appropriate model parameters (resistance and compliance) for outlet pressure waveforms poses challenges in the absence of in vivo pressure data.

In this study, a methodology was developed to ascertain WK2 model parameters without relying on in vivo pressure measurements, utilizing an analytical solution outlined in Supplementary S4. This technique is termed the maximum admittance method (MAM), which leverages the WK2 model (WK2-MAM). Admittance (the inverse of impedance) facilitates the evaluation of composite impedance across parallel arterial networks (as portrayed in Fig. 2), where the maximum peripheral admittance corresponds to the lowest impedance to the peripheral regions of the arterial network. The physical meaning of minimum impedance is to determine optimized flow divisions in terms of energy consumption during fluid transport, similar to Murray's law. Using the determined lumped parameters, the pressure waveforms can be directly imposed at the outlets through the analytical solution (expressed in Supplementary Eq. (S10)). Ideally, this approach enables the application of standard (not in vivo) pressure waveforms to both healthy and stenotic cerebrovascular networks for the hemodynamic study regarding the geometrical effect of arteries.

The peripheral admittance is defined as follows:

$$Y_{ph} = \frac{1}{Z_{ph}} = Y_{ACA} + Y_{MCA1} + Y_{MCA2} \quad (4)$$

where

$$Y_{ACA} = \frac{1}{R_{ACA}} + j\omega C_{ACA}, \quad (5)$$

$$Y_{MCA1} = \frac{1}{R_{MCA1}} + j\omega C_{MCA1}, \text{ and} \quad (6)$$

$$Y_{MCA2} = \frac{1}{R_{MCA2}} + j\omega C_{MCA2}. \quad (7)$$

In Eqs. (5)–(7), $j^2 = -1$ and $\omega = 2\pi/T$. The magnitude of the peripheral admittance, which is the objective function for optimizing the lumped parameters, is calculated as follows:

$$\|Y_{ph}\| = \sqrt{\left(\frac{1}{R_{ACA}} + \frac{1}{R_{MCA1}} + \frac{1}{R_{MCA2}}\right)^2 + \omega^2(C_{ACA} + C_{MCA1} + C_{MCA2})^2}. \quad (8)$$

Figure 4 depicts a flowchart of the WK2-MAM. The volumetric flow rates through the ICA (Q_{ICA}), systolic pressure (P_s), diastolic pressure (P_d), and sets of cycle-averaged flow division ratios ($\{\overline{Q}_{ACA}/\overline{Q}_{MCA}\}$ and $\{\overline{Q}_{MCA2}/\overline{Q}_{MCA1}\}$) were used as the input values. The systolic and diastolic pressures were used to calculate the lumped parameters. With reference to Supplementary Eqs. (S11) and (S12), the systolic and diastolic pressures are expressed using the ICA volumetric flow rates (in Eq. (3))

$$P_s = a_0R + TR \sum_{n=1}^8 \left[\frac{(Ta_n - 2n\pi RCb_n) \cos\left(\frac{2n\pi t_s}{T}\right) + (2n\pi RCa_n + Tb_n) \sin\left(\frac{2n\pi t_s}{T}\right)}{T^2 + (2n\pi RC)^2} \right] \text{ and} \quad (9)$$

$$P_d = a_0R + TR \sum_{n=1}^8 \left[\frac{Ta_n - 2n\pi RCb_n}{T^2 + (2n\pi RC)^2} \right] \quad (10)$$

where the Fourier coefficients (a_n and b_n , $n \geq 1$) are listed in Table 2. The cycle-averaged volumetric flow rates for each artery ($a_{0,ACA}$, $a_{0,MCA1}$, and $a_{0,MCA2}$) were derived from the cycle-averaged flow division ratios utilized as the input values. By simultaneously solving Eqs. (9) and (10) based on the specified systolic and diastolic pressures, the resistance and compliance could be calculated for each arterial branch, respectively.

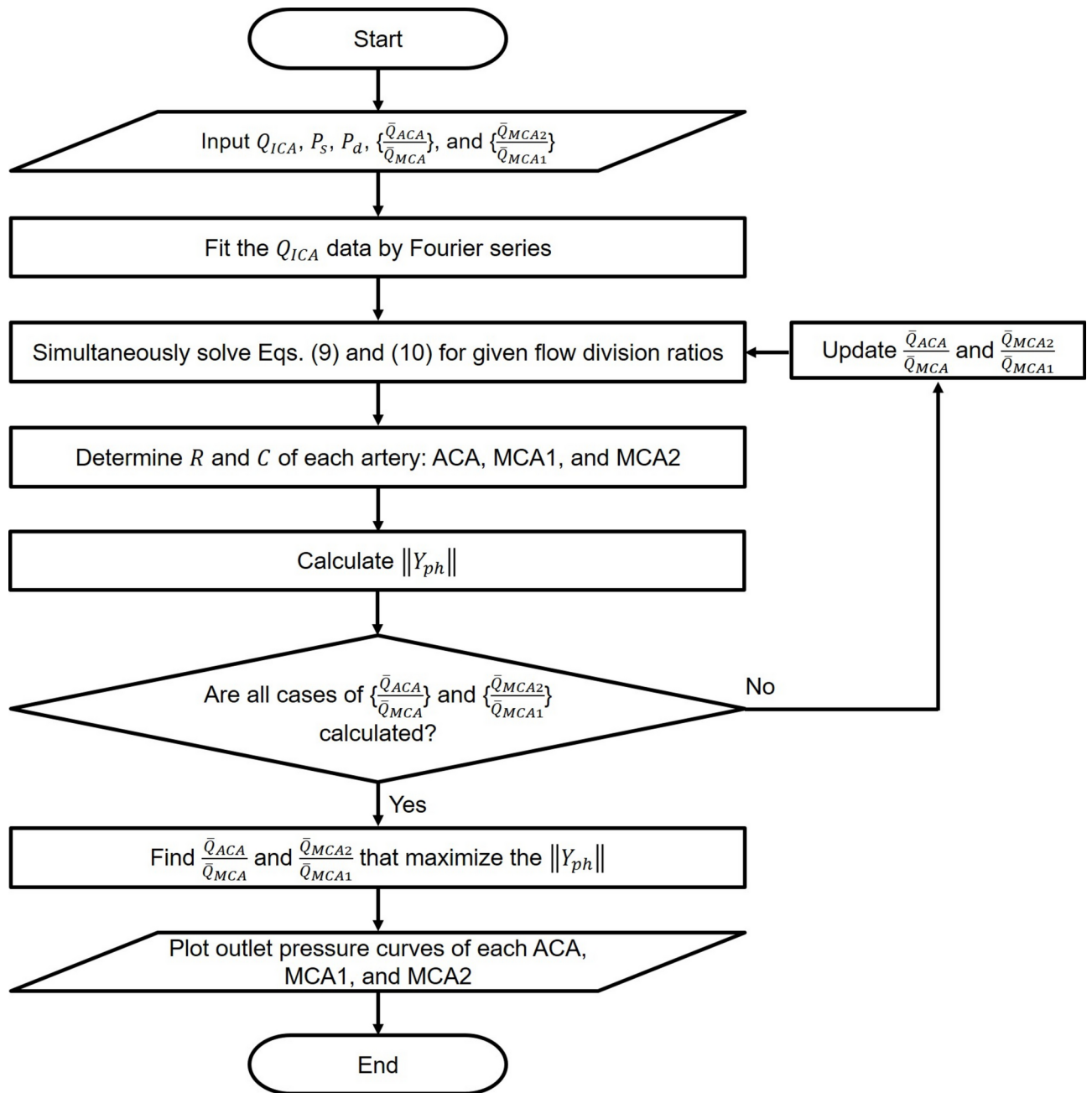


Fig. 4. Flow chart of the WK2-MAM.

Iterative computations were conducted using MATLAB to determine the flow division ratios that maximized peripheral admittance. The iterative calculations for determining the lumped parameters began with the initial values set to zero. The computations converged within several hundred iterations, with the residuals falling below a tolerance of 10^{-5} .

In the WK2-MAM, the phase lag was neglected. The order of the length scale along the flow direction in CFD domain was 10^{-2} m, and the order of magnitude of the pulse wave velocity was estimated as 10^1 m/s using the Moens–Korteweg formula. Therefore, the phase lag was minor as the order of magnitude was 10^{-3} s, which is extremely small when compared with the cardiac cycle period (≈ 1 s). A negligible phase lag indicates that the Fourier coefficients determined by the ICA volumetric flow rates (a_n and b_n in Eq. (3), $n \geq 1$) are preserved and can be used to describe the flow rate waveforms of ACA, MCA1, and MCA2. Therefore, only the cycle-averaged flow rates (a_0 in Eq. (3)) differ depending on the flow divisions at the arterial bifurcations; thus, the peripheral admittances are calculated by altering $\bar{Q}_{ACA}/\bar{Q}_{MCA}$ and $\bar{Q}_{MCA2}/\bar{Q}_{MCA1}$.

For normal blood pressure, the systolic and diastolic pressures were assumed to be 110 mmHg and 70 mmHg, respectively. Figure 5 plots contour charts of the normalized admittance ($\|Y_{ph}\|/\|Y_{ph}\|_{max}$) depending on the cycle-averaged flow division ratios. As depicted, the optimal flow division ratios were

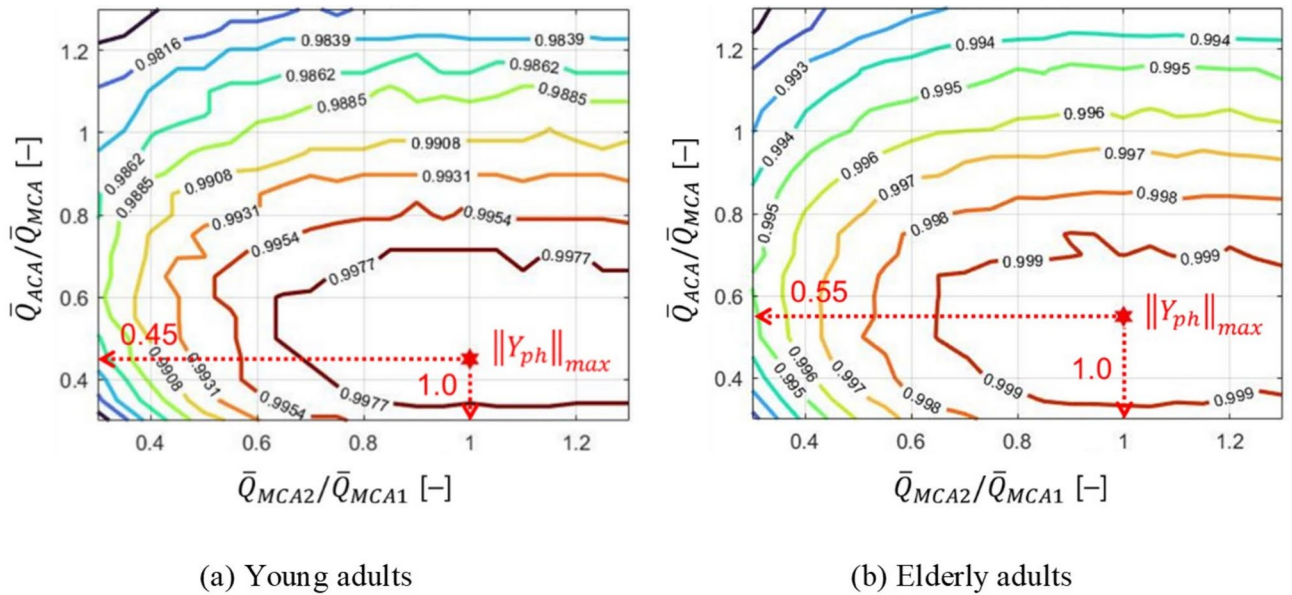


Fig. 5. Contours of normalized peripheral admittance.

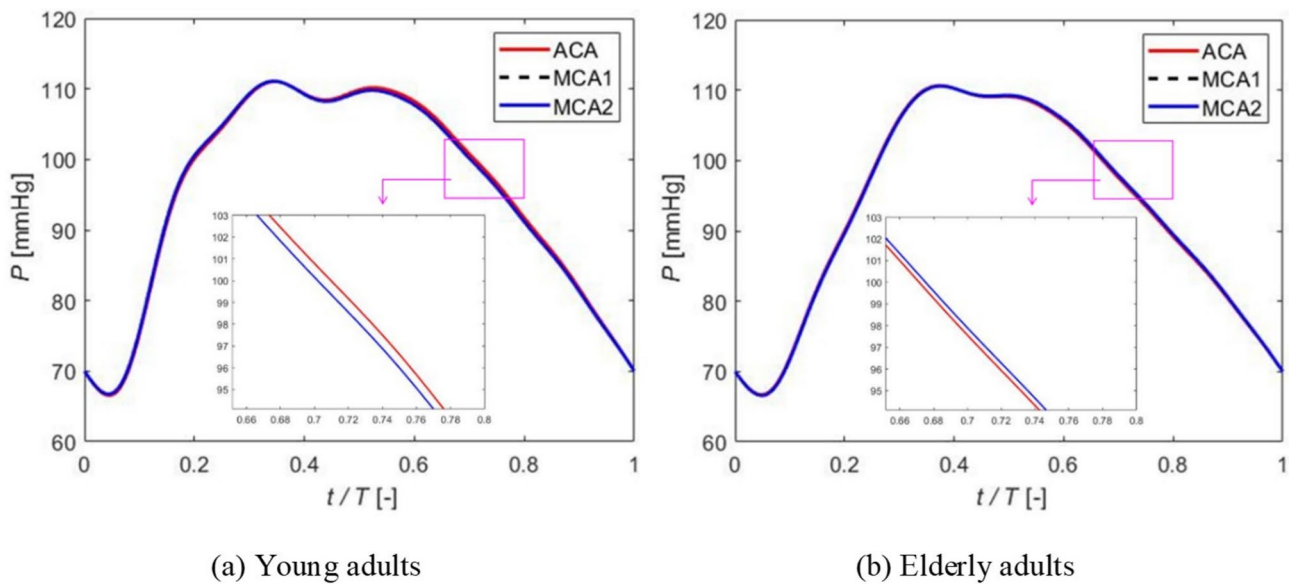


Fig. 6. Pressure curves for outlet boundary conditions.

estimated as $\bar{Q}_{ACA}/\bar{Q}_{MCA} = 0.45$, $\bar{Q}_{MCA2}/\bar{Q}_{MCA1} = 1.0$ for young adults and $\bar{Q}_{ACA}/\bar{Q}_{MCA} = 0.55$, $\bar{Q}_{MCA2}/\bar{Q}_{MCA1} = 1.0$ for elderly adults.

To validate the reliability of WK2-MAM, the estimated flow division ratios ($\bar{Q}_{ACA}/\bar{Q}_{MCA}$) were compared with the measured in vivo values using phase-contrast magnetic resonance imaging (PCMRI) in healthy adults. Based on the mean blood flow rates⁴³, the ACA-to-MCA flow division ratios were calculated as 0.55 and 0.57 for young (49 people) and elderly (45 people) adults, respectively. However, the PCMRI data for $\bar{Q}_{MCA2}/\bar{Q}_{MCA1}$ have not been reported previously⁴³. The estimated values of $\bar{Q}_{ACA}/\bar{Q}_{MCA}$ are consistent with the PCMRI data, within 18% and 3.5% relative errors for young and elderly adults, respectively. The estimated flow division ratios are expected to lie within the standard deviations (17%–23% of mean values) of the measured blood flow rates in MCA and ACA⁴³. Additionally, the ACA-to-MCA flow division ratio based on the mean volumetric flow rates of healthy adults obtained from numerous studies is 0.5⁴⁴. Therefore, the WK2-MAM can produce clinically reasonable flow division ratios.

The pressure curves for the young and elderly adults, utilized as outlet boundary conditions, are depicted in Fig. 6a, b, respectively. Figure 6 shows that the outlet pressure curves for the ACA and MCA, derived from the

WK2-MAM, exhibited no significant differentiation, given that the $\bar{Q}_{ACA}/\bar{Q}_{MCA}$ ratios were approximately 0.5 for both age groups. With $\bar{Q}_{MCA2}/\bar{Q}_{MCA1} = 1.0$, the pressure curves for MCA1 and MCA2 coincided.

CFD results and discussion

Hemodynamic analysis regarding the physiological factors

Figure 7 visualizes cycle-averaged 3-D flow structures within the MCA for medium viscosity blood (4.3 mPa·s) based on the flow waveform for elderly adults. In the healthy MCA (Fig. 7a), the blood flow was smooth, whereas recirculating flows emerged after stenosis progression (Fig. 7b–d). As the narrow lumen from severe stenosis increased the flow resistance towards the MCA, the blood preferentially flowed towards the ACA rather than the MCA (Supplementary Figs. S5(a)–(b)). To mitigate the blood supply deficits, reverse flows were induced in the MCA2 branch (Fig. 7d, Supplementary Fig. S5(c)), given equivalent outlet pressure waveforms as opening boundaries for the MCA1 and MCA2 branches (as depicted in Fig. 6). The reverse flows, observable under flow waveforms for young adults as well, were utilized as a criterion of identifying the occurrence of MCA ischemia. In the cases of moderate stenosis, the mass flow rates to the ACA were higher than those to the MCA (Supplementary Fig. S5(d)).

Figure 8 depicts the NRRT contours for cerebrovascular networks, derived from the flow waveform of elderly adults. NRRT values below 1.0 (depicted as dark blue zones in Fig. 8) indicate shorter particle residence times compared to the fully developed Hagen–Poiseuille flow at the ICA inlet. For networks with healthy (Fig. 8a,b) and normal-mildly stenotic MCAs (Fig. 8c,d), longer residence times were anticipated at the curved sections of the ICA (* locations) instead of at the bifurcated branches near the MCA (outlined by pink-dotted boxes).

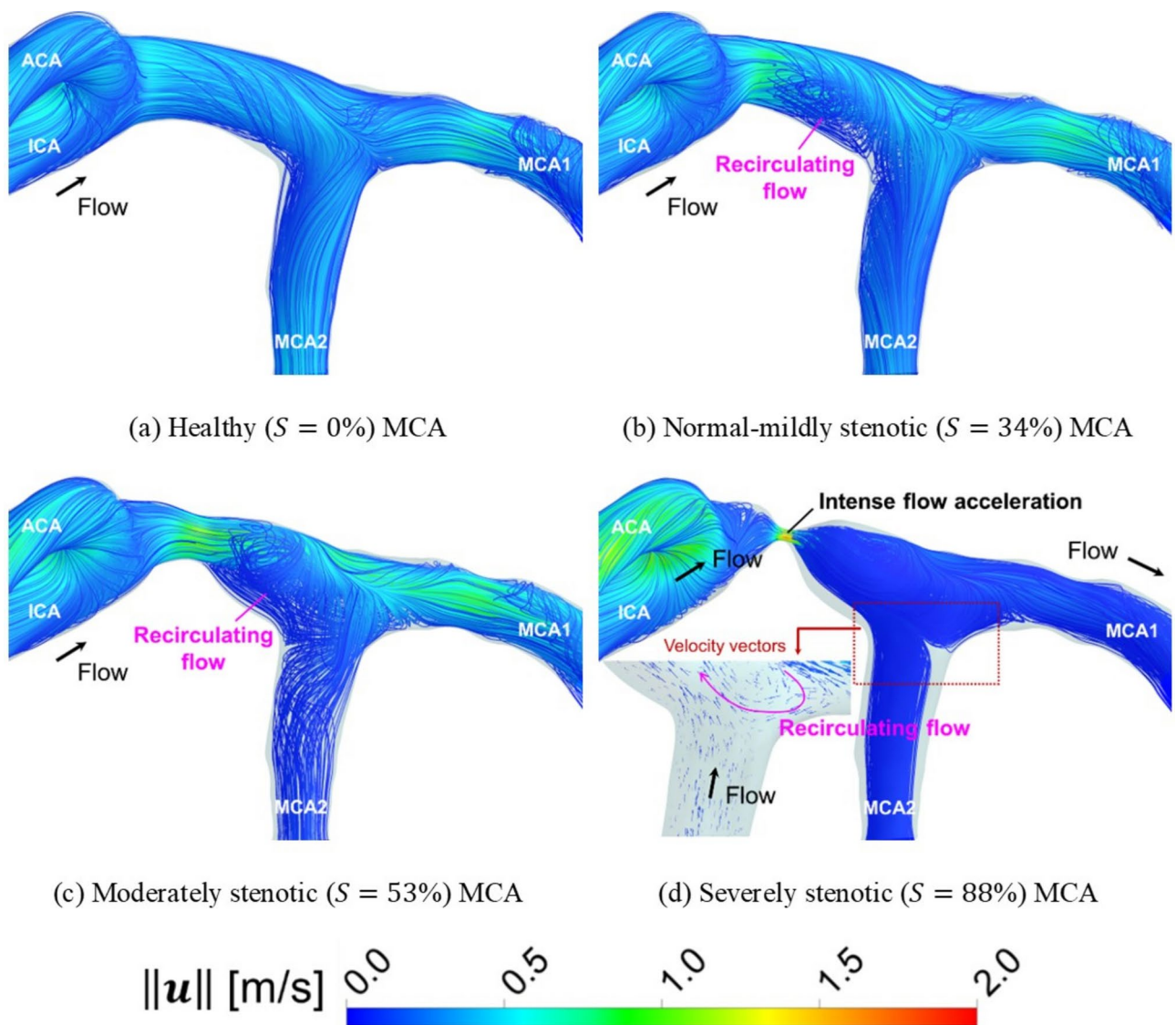


Fig. 7. Cycle-averaged 3-D flow structures (elderly adults, viscosity 4.3 mPa·s). In the case of 88% severity, reverse blood flow in the MCA2 branch was a criterion for identifying ischemia occurrence.

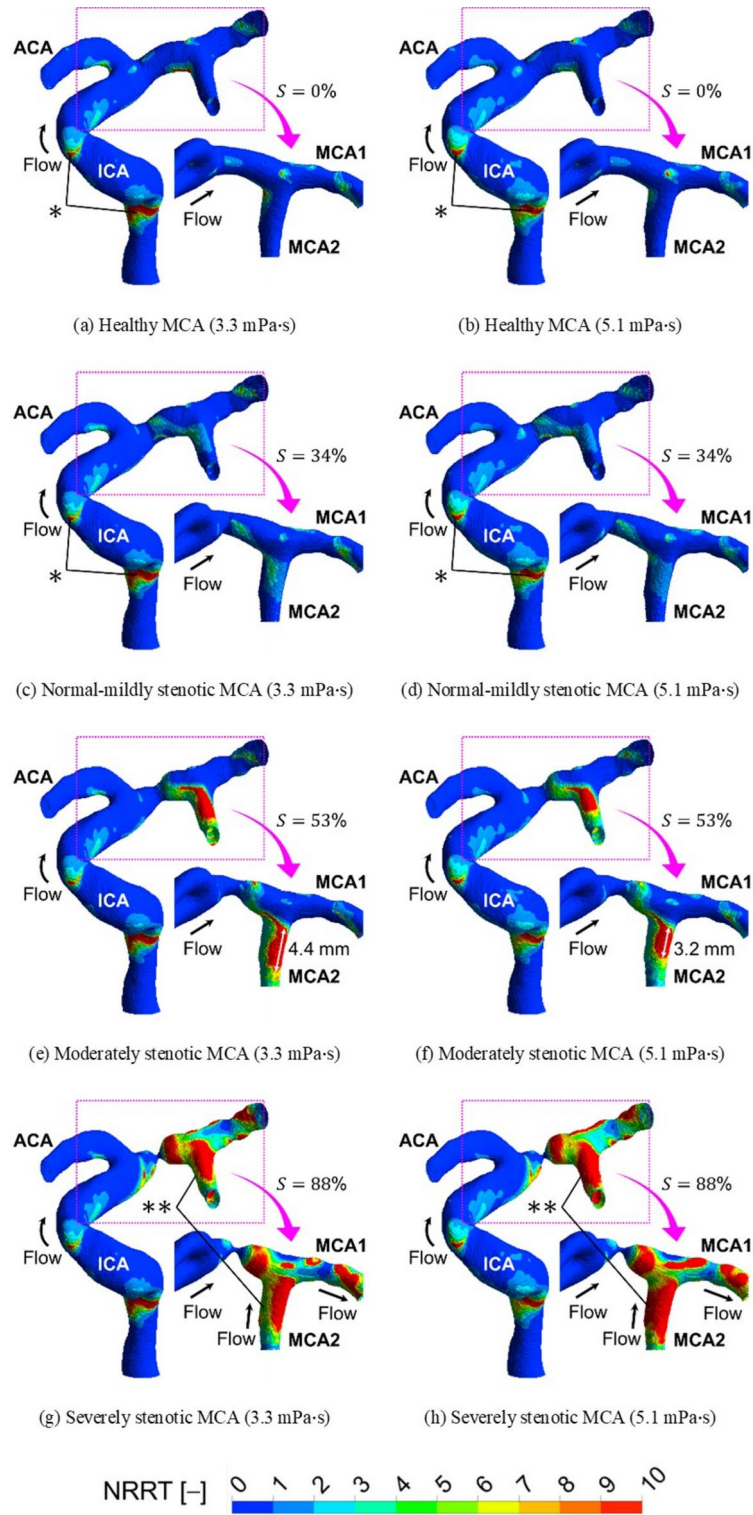


Fig. 8. Normalized relative residence time (NRRT) contours calculated from the flow waveform of elderly adults.

Thus, the curvature of the cerebral arteries significantly contributes to the localization of atherosclerotic lesions in arteries that are either clear or mildly obstructed. Conversely, for moderately stenotic MCAs (Fig. 8e,f), the residence time in the MCA2 branch significantly increased due to the elevated flow resistance from the stenosis, which impeded the blood supply.

A comparison of the NRRT contours between low (Fig. 8a,c) and high (Fig. 8b,d) blood viscosities within the clinically acceptable range (3.3–5.1 mPa·s) reveals that changes in the blood viscosity do not significantly

affect NRRT for mild stenosis severity. However, in the cases of moderate MCA stenosis, low-viscosity blood led to a 37.5% increase in the length of the red-colored zone at the MCA2 branch (4.4 mm in Fig. 8e) when compared with high-viscosity blood (3.2 mm in Fig. 8f). This is because low-viscosity blood is more inertia-dominant and predominantly flows through the MCA1 branch, thus reducing the flow to the MCA2 branch and consequently increasing NRRT. In the cases of severe stenosis, the increased viscosity resulted in reduced reversed flow from the MCA2 branch (as portrayed in Supplementary Fig. S5(c)), which increased the NRRT for high-viscosity blood (** locations in Fig. 8h) beyond that for low-viscosity blood (** locations in Fig. 8g). Thick atherosclerotic plaques are strongly associated with elevated levels of LDL⁴⁵, and the LDL concentration inversely correlates with WSS magnitude⁴⁶. Although the blood viscosity affects the particle residence time, LDL concentration is predominantly influenced by arterial geometry (e.g., curvature, stenosis severity, bifurcation) over blood viscosity, as indicated by the NRRT analyses.

The inverse correlation between the cycle-averaged WSS and OSI corresponds to tissue degradation and damage of vascular walls⁴⁷. However, it is difficult to visualize the correlation based on the stenosis severity since the stenosis progression alters the vascular geometry. To quantify any correlation, changes in the cycle-averaged WSS and OSI must be evaluated at the same site. Therefore, we computed ECAP (Table 1) to identify and visualize simultaneous changes in the WSS and OSI, along with stenosis severity variations.

Figure 9 depicts the ECAP contours calculated from the flow waveform of elderly adults. Low-level ECAP was produced within a blood viscosity range (3.3–5.1 mPa·s) for normal-mildly stenotic MCAs, as shown in Fig. 9a,b. As the stenosis grows to a moderate state (Fig. 9c,d), the ECAP was significantly increased at the MCA2 branch, which indicates low WSS and high OSI at the positions. Furthermore, the low-viscosity blood (Fig. 9c) increased the ECAP in a wider area when compared with that of the high-viscosity blood (Fig. 9d) at the MCA2 branch. Similar to the NRRT analyses (Fig. 8e,f), this is attributed to the reduction in the flow to the MCA2 branch for the low-viscosity blood due to inertial effects.

Figure 10 depicts the normalized cycle-averaged WSS and OSI contours to demonstrate the inverse correlation at the MCA2 branch. The hemodynamic indices were computed from the flow waveform of elderly adults with high-viscosity blood. Both the WSS and OSI are low at the MCA2 branch (* locations) for normal-mildly stenotic MCAs, as shown in Fig. 10a,c. At the same positions (* locations in Fig. 10b,d), the MCA2 vascular walls experience much lower WSS and higher OSI when the stenosis progressed to the moderate state. Consequently, an inverse correlation was observed at the MCA2 branch with the stenosis progression from the normal-mild to moderate states. This inverse correlation intensified for low-viscosity blood owing to the predominant flows through the MCA1 branch.

Conversely, the severely stenotic MCAs (Fig. 9e,f) produced lower ECAP when compared with the moderately stenotic MCAs (Fig. 9c,d) at the MCA2 branch. These results can be attributed to the low values of both cycle-averaged WSS and OSI at the post-stenosis region owing to the occurrence of ischemia. High WSS is induced at the ACA branch since most of the blood flows to the ACA (Supplementary Fig. S5(a)), as shown in Fig. 11a,b. In the post-stenosis region, the normalized cycle-averaged WSS is below 1 at most vascular walls, which is comparable to OSI. Therefore, the ECAP approaches unity after it is defined (Table 1). For the severely stenotic MCA, high-viscosity blood (Fig. 9f) produced higher ECAP when compared with low-viscosity blood (Fig. 9e) in the post-stenosis region. This is attributed to the higher OSI for the high-viscosity blood (Fig. 11d) when compared with the low-viscosity blood (Fig. 11c).

However, when the stenosis progressed from the moderate to severe states, an inverse correlation was observed at the MCA1 branch. The ECAP at the MCA1 branch increased as the stenosis progresses from moderate (Fig. 9d) to severe (Fig. 9f) levels. Furthermore, the cycle-averaged WSS decreased to less than 10% at the MCA1 branch (** locations in Fig. 10b and 11b) and the OSI increased sharply at the same sites (** locations in Fig. 10d and 11d). The flow waveform of young adults also produced similar inverse correlations at the MCA1 (stenosis severity: 53% → 88%) and MCA2 (stenosis severity: 34% → 53%) branches. For the simulation results, an inverse correlation was observed between the cycle-averaged WSS and OSI in the post-stenosis regions along with the stenosis progression. This inverse correlation may cause further damage to the vascular walls in the post-stenosis zones.

A low FPR indicates a heightened risk of ischemia¹⁴. Accordingly, the FPR contours of high-viscosity blood (5.1 mPa·s) were obtained on the flow waveform of young adults (Fig. 12a–c), presenting the lowest values corresponding to equivalent stenosis severity due to high \bar{Q}_{ICA} (as depicted in Fig. 3). Until moderate stenosis, the FPR values in post-stenosis regions did not significantly decrease (Fig. 12a,b), although they locally fall below 0.9 (* locations in Fig. 12b). Conversely, the FPR values in the post-stenosis zones remarkably decreased between 0.8 and 0.85 in cases of severe occlusion, irrespective of the flow waveform (Fig. 12c,d). The calculated FPR values of the severe occlusion cases appear to be relatively large when compared to the measured data¹⁴, as shown in Supplementary Fig. S6. However, the measured FPRs are broadly distributed for equivalent stenosis severity (Supplementary Fig. S6). This can be attributed to the varying blood flow rates and the arterial shapes of each individual. The reliability of the simulation results was determined based on the broad distributions of the FPRs despite similar severity levels. The effect of viscosity changes on the FPR is further elaborated in Section “Discussion on the influence of flow waveform and blood viscosity”.

In terms of plaque rupture, the pressure force plays a more dominant role than the shear force⁴⁸. Figure 13 depicts the cycle-averaged values of the maximum pressure gradient magnitude on the stenotic walls ($\overline{\|\nabla P\|_{max}} = \int_0^T \|\nabla P\|_{max} dt / T$). Owing to the flow acceleration in the narrowed lumen, the magnitude of the pressure gradient vector significantly increased at the stenotic walls. As illustrated in Fig. 13, the maximum pressure gradient points were located at the shoulder of the stenosis, where the magnitudes of the pressure gradient vectors were probed.

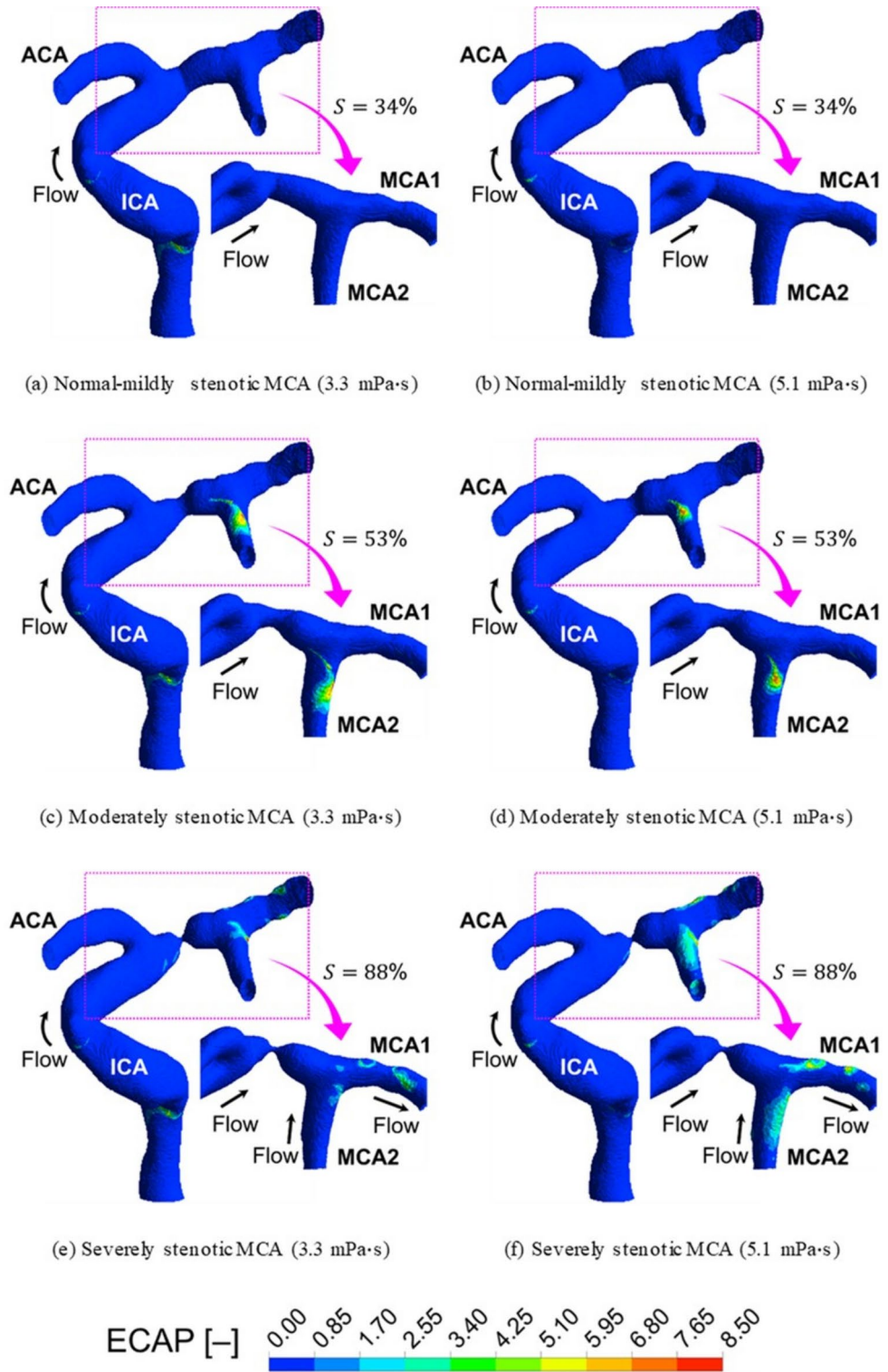


Fig. 9. Endothelial cell activation potential (ECAP) contours calculated from the flow waveform of elderly adults.

Comparing $\overline{\|\nabla P\|_{max}}$ of young (Fig. 13a) and elderly (Fig. 13b) adults, high \overline{Q}_{ICA} of young adults (Fig. 3) resulted in higher pressure force on the stenosis wall than elderly adults. Moreover, the increased viscosity subjected fluid elements to a higher pressure force for an equivalent volumetric flow rate, thus enhancing the $\overline{\|\nabla P\|_{max}}$ with blood viscosity.

The $\overline{\|\nabla P\|_{max}}$ increases with the stenosis severity, as shown in Fig. 13. Specifically, with the stenosis progression from the moderate to severe states, the $\overline{\|\nabla P\|_{max}}$ values increased by a factor of approximately 6.7

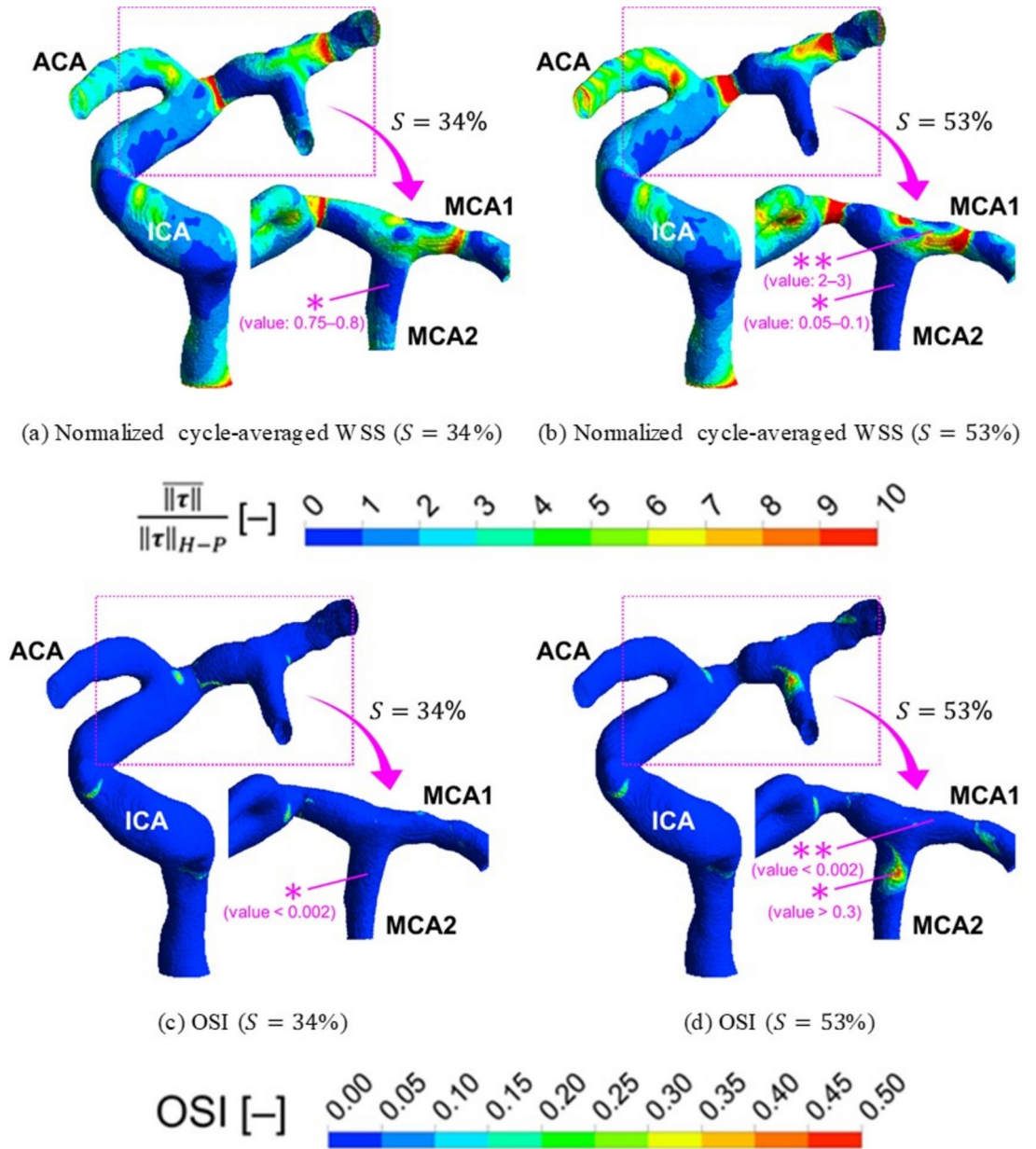


Fig. 10. Hemodynamic indices calculated from the flow waveform of elderly adults (5.1 mPa·s).

when compared to those of moderate stenosis. This originates from the local extreme flow acceleration in the narrowest lumen of the severe stenosis (Fig. 7d), which indicates a high probability of plaque rupture.

Discussion on the influence of flow waveform and blood viscosity

Given the inherent inaccuracies and resolution limitations of time-resolved 3-D PCMRI data, the precise quantification of hemodynamics near vascular walls poses challenges⁴⁹. To quantitatively assess the impact of the flow waveform on the NRRT, the relative difference was defined as follows:

$$RD_{w, NRRT} = \frac{|NRRT_Y - NRRT_E|}{NRRT_E} \times 100. \tag{11}$$

Figure 14 depicts the relative difference contours of NRRT associated with the flow waveform variations. In normal-mildly stenotic arterial networks, most relative differences were below 15% across a viscosity range of 3.3–5.1 mPa·s (Fig. 14a,b). Similar $RD_{w, NRRT}$ values were observed in healthy networks, suggesting that NRRT consistently identified high-risk atherosclerosis locations despite varying flow waveforms, thereby serving as a robust hemodynamic index that is resistant to flow rate uncertainties.

However, the reliability of NRRT was significantly compromised by the flow waveform variations as stenosis progressed. For example, relative differences surpassed 30% at the MCA2 branch in the cases of moderate

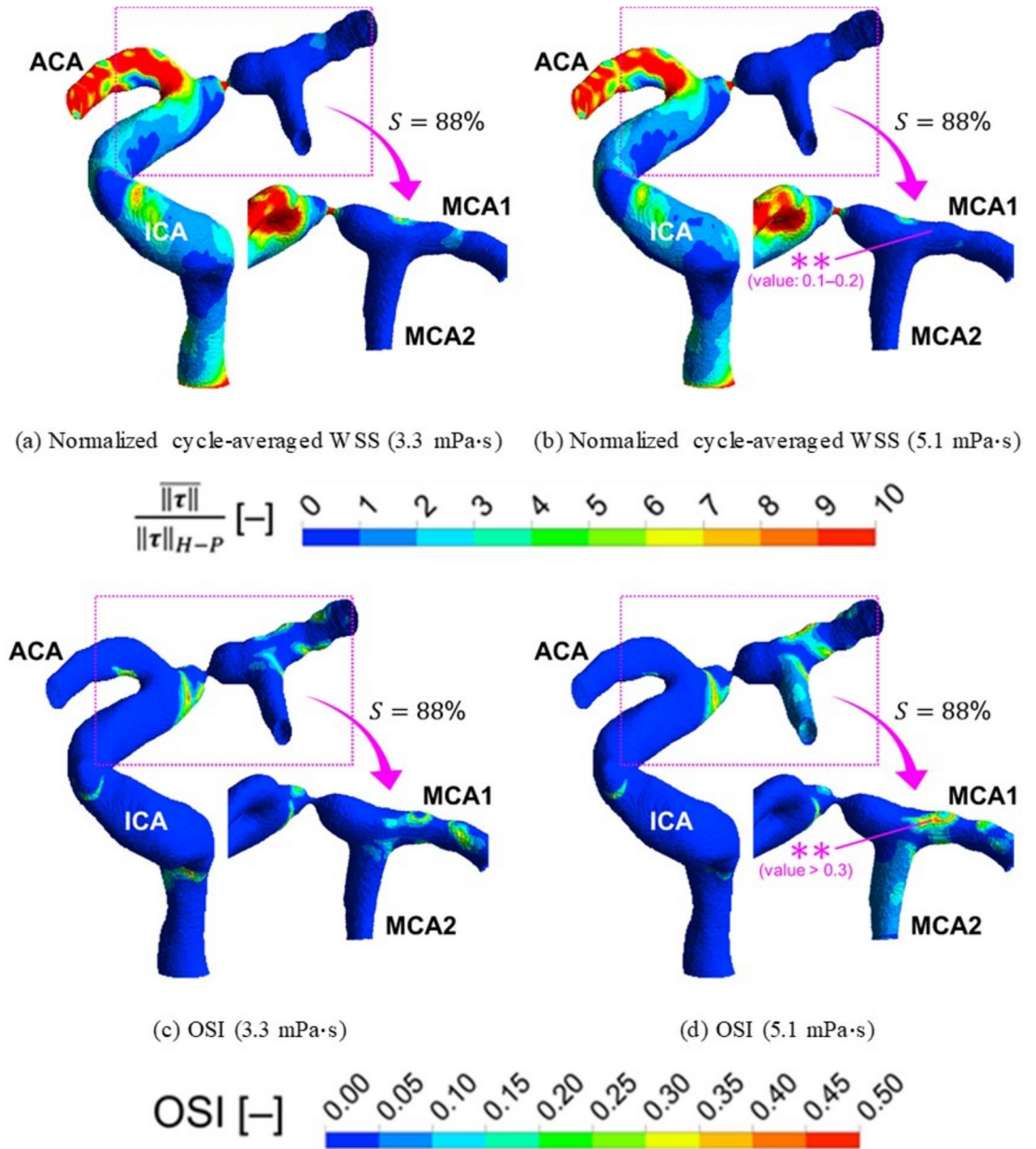


Fig. 11. Hemodynamic indices of severely stenotic MCA calculated from the flow waveform of elderly adults.

stenosis with low-viscosity blood (Fig. 14c). Moreover, for severe stenosis, the relative differences escalated at both the MCA1 and MCA2 branches with high-viscosity blood (Fig. 14f), thus indicating that NRRT lost its robustness as a hemodynamic index for analyzing stenotic arteries when the severity exceeded 50%.

In the MCA2 branch, low-viscosity blood exhibited higher relative differences ($RD_{w,NRRT}$) for moderate stenosis (Fig. 14c) and lower relative differences for severe stenosis (Fig. 14e) when compared to those observed with high-viscosity blood. Given that NRRT is affected by the magnitude and oscillation of WSS vectors across a cardiac cycle (as outlined in Table 1), the contrasting results based on blood viscosity are complex to interpret. Nonetheless, the cycle-averaged mass flow rates through the MCA2 branch decreased and increased for moderate and severe stenosis, respectively, with a decrease in the blood viscosity (Supplementary Fig. S5(c)). Consequently, the sensitivity of NRRT to the flow waveform variations increased significantly where the mass flow rate is reduced. Additionally, with the occurrence of ischemia, the low mass flow rate of elderly adults with high-viscosity blood presents a high risk of atherosclerotic plaque formation due to the enhanced residence time near the vascular walls (Supplementary Fig. S7).

Furthermore, the viscosity-related relative difference was defined to evaluate the effect of the viscosity increment as follows:

$$RD_{v,h} = \frac{h_{high} - h_{low}}{h_{low}} \times 100, \tag{12}$$

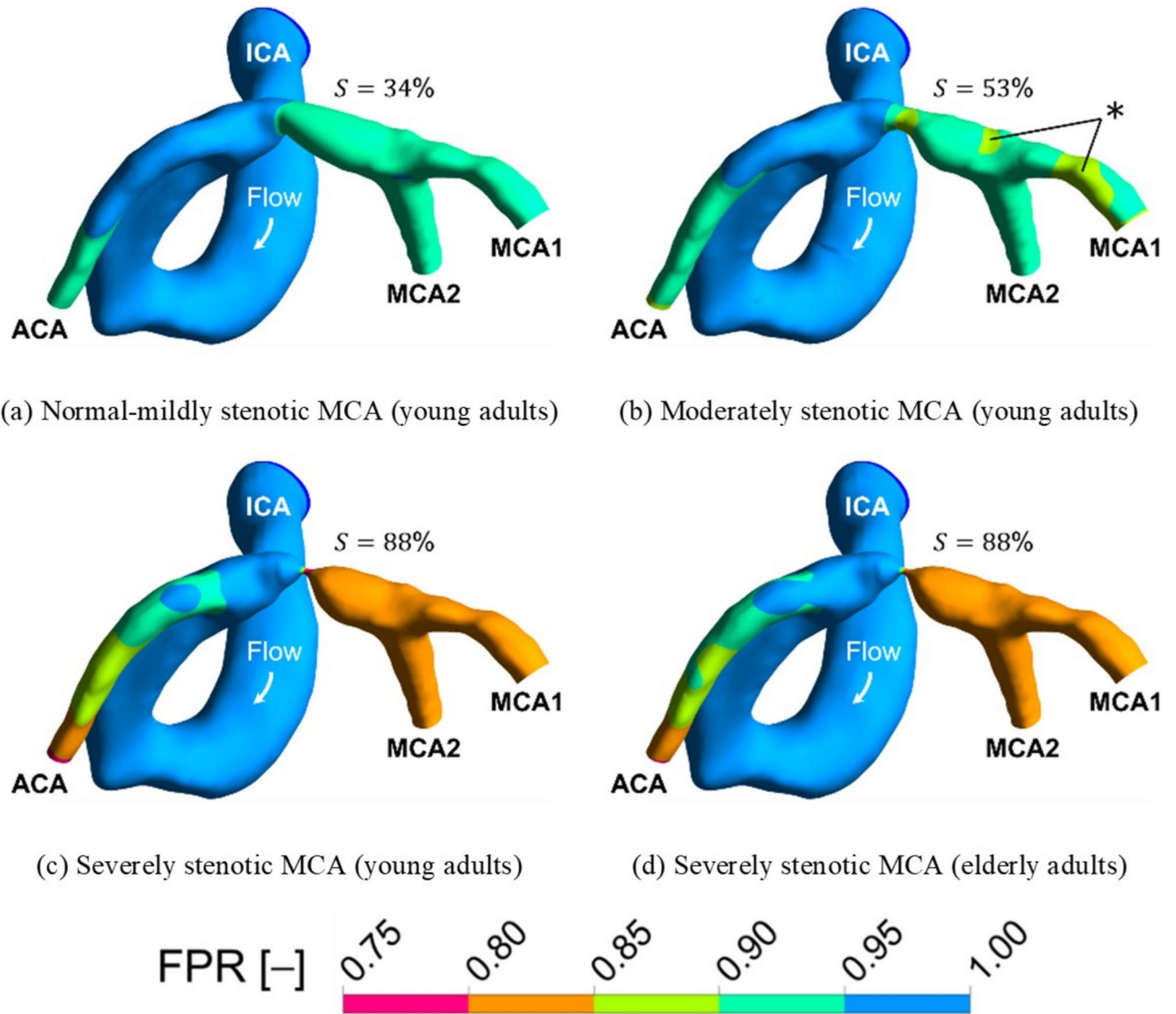


Fig. 12. Fractional pressure ratio (FPR) contours of high-viscosity blood (5.1 mPa·s).

where h denotes an arbitrary quantity such as FPR or $\|\nabla P\|_{max}$. Figure 15 presents contours of the viscosity-related relative difference of FPR ($RD_{v,FPR}$) derived from the flow waveform of young adults (viscosity transition: 3.3 \rightarrow 5.1 mPa·s). Because the FPR decreased with increment of the blood viscosity due to heightened flow resistance, the relative difference values were negative.

As shown in Fig. 15a,b, the absolute values of $RD_{v,FPR}$ remained below 1% for normal-mildly stenotic conditions, despite a 54.5% increase in blood viscosity (3.3 to 5.1 mPa·s). Although the absolute values of $RD_{v,FPR}$ in the distal regions increased with the stenosis severity (Fig. 15b–d), they remained under 3% even at 88% stenosis severity (Fig. 15d), indicating the near-independence of FPR from viscosity. The $RD_{v,FPR}$ contours associated with flow waveforms from elderly adults mimicked those depicted in Fig. 15, affirming the effectiveness of FPR as an indicator of vessel occlusion across varying viscosities under specific blood flow scenarios.

Figure 16 illustrates the viscosity-related relative differences in the cycle-averaged maximum pressure gradient ($RD_{v,\|\nabla P\|_{max}}$). With a 54.5% increase in the blood viscosity (from 3.3 to 5.1 mPa·s), the $\|\nabla P\|_{max}$ exhibits less than a 9% increase across all the simulated stenotic MCAs (Fig. 16), indicating a marginal impact of viscosity on the maximum pressure gradient and suggesting minor influence on the plaque rupture risk. Additionally, despite stenosis progression from 53 to 88% severity, the $RD_{v,\|\nabla P\|_{max}}$ values remained almost unchanged for both the young (from 8.4% to 8.4%) and elderly (from 8.9% to 9%) adult flow waveforms. These findings suggest that the increase in blood viscosity exerted a consistent effect on the normal stress on stenotic walls (fibrous cap), irrespective of the stenosis severity, once the severity exceeded 50%.

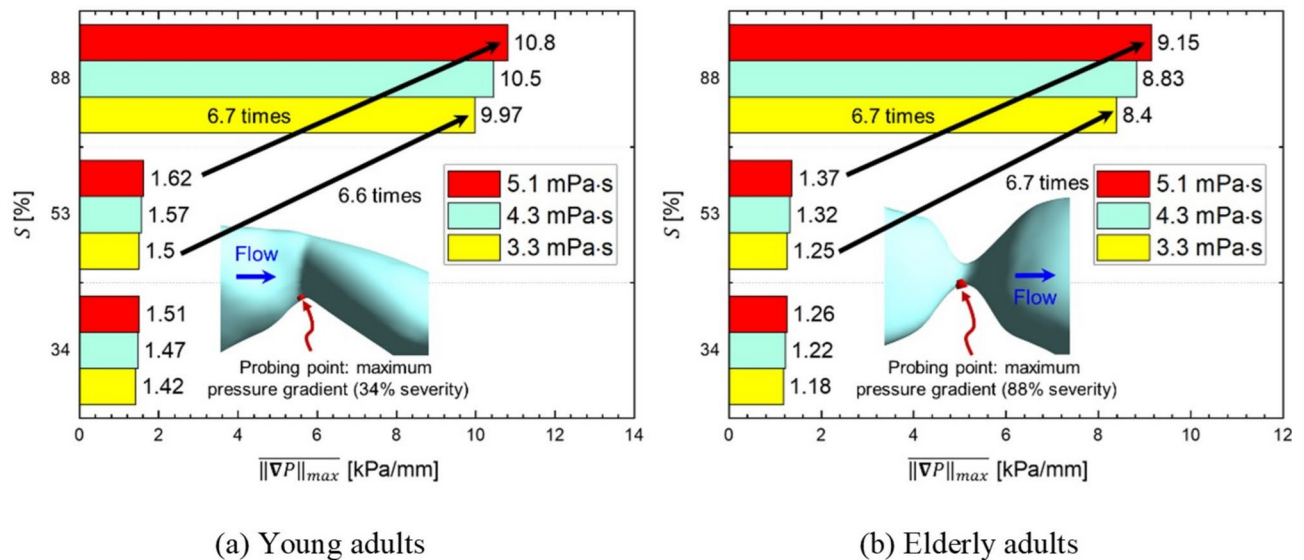


Fig. 13. Cycle-averaged values of the maximum pressure gradient magnitude on stenotic walls.

Limitations

This study had some limitations owing to the simplification of the problem. Firstly, the CFD simulations were performed while assuming laminar flows of Newtonian fluids. Nevertheless, the assumptions employed in this study adequately simplified the simulations for investigating the cerebral artery hemodynamics owing to a negligible shear-thinning effect of arterial-scale blood flows^{26,27} and weak turbulence in the post-stenosis zone (Supplementary Fig. S1).

Secondly, small ROIs were considered in both the WK2-MAM development and CFD simulations. As mentioned in Section “Outlet: pressure waveform derived from maximum admittance method based on two-element Windkessel model (WK2-MAM)”, the phase lag was neglected in the development of WK2-MAM; this limits the applicability of the proposed method to a small domain. As the size of the ROI increased, the discrepancy of the flow waveforms between the proximal and distal regions was not negligible. Accordingly, the CFD domains were produced by segmenting the entire reconstructed cerebral artery networks. In terms of the blood flow distributions in arterial networks, resolving large-scale ROI with numerous branches would be favorable. However, in this study, we aimed to analyze the influence of the various physiological factors on hemodynamics near the stenotic location; thus, the ROI was segmented to minimize the computational cost. Nonetheless, the segmented ROI could result in appropriate blood flow distributions (Supplementary Fig. S8).

Thirdly, the fluid–structure interaction was not considered in this study. Because the blood vessels are soft, a considerably realistic hemodynamic analysis can be achieved by considering the interaction of blood flows and wall deformations, such as tardus-parvus effect in post-stenosis region⁵⁰. However, rigid wall assumptions have also been used for blood flow simulations owing to the insignificant effect of wall deformations⁵¹. The effects of fluid–structure interaction become increasingly prominent with increasing blood pressure⁵². Consequently, in this study, which considered a normal blood pressure range, the rigid wall assumption facilitated sufficiently accurate hemodynamic analyses while considerably reducing the computational cost.

Conclusions

In this study, a numerical investigation into the hemodynamics of cerebrovascular networks was conducted with focus on the progression of MCA stenosis under varying blood viscosities and flow waveforms. To alleviate the computational demands of iterative 3-D CFD simulations for achieving optimal flow divisions according to the MEL principle, the WK2-MAM was introduced to set the outlet pressure boundary conditions in arterial networks. The pressure waveforms can be directly applied at the outlet boundaries by the analytical solution of the WK2 model. The WK2-MAM effectively simplified the determination of outlet pressure boundary conditions for the investigation of hemodynamic characteristics affected by various physiological factors such as stenosis severity, blood viscosity, and flow rates without requiring in vivo pressure measurements.

We assessed 3-D flow structures, blood flow distributions, NRRT, ECAP, cycle-averaged WSS, OSI, FPR, and maximum pressure gradients. Investigating the effects of physiological factors, the stenosis severity emerged as the primary factor influencing hemodynamics by initiating recirculating or reverse flows in the post-stenosis region. Severely stenotic MCAs with an 88% severity level were predicted to induce ischemia irrespective of blood viscosity and flow waveform. Until a severity level of 34%, the NRRT distributions remained consistent within 15% between the two flow waveforms, highlighting its reliability in identifying atherosclerosis risk locations. Nonetheless, beyond 50% severity, the NRRT sensitivity to flow variations increased, diverting more blood towards the ACA rather than the MCA. Therefore, a 50% severity level was identified as a crucial juncture, marking a significant shift in the hemodynamic behavior from that observed in healthy cerebral arteries. Under the ischemia situation (88% severity), the elderly adults with high-viscosity blood produced NRRT that is

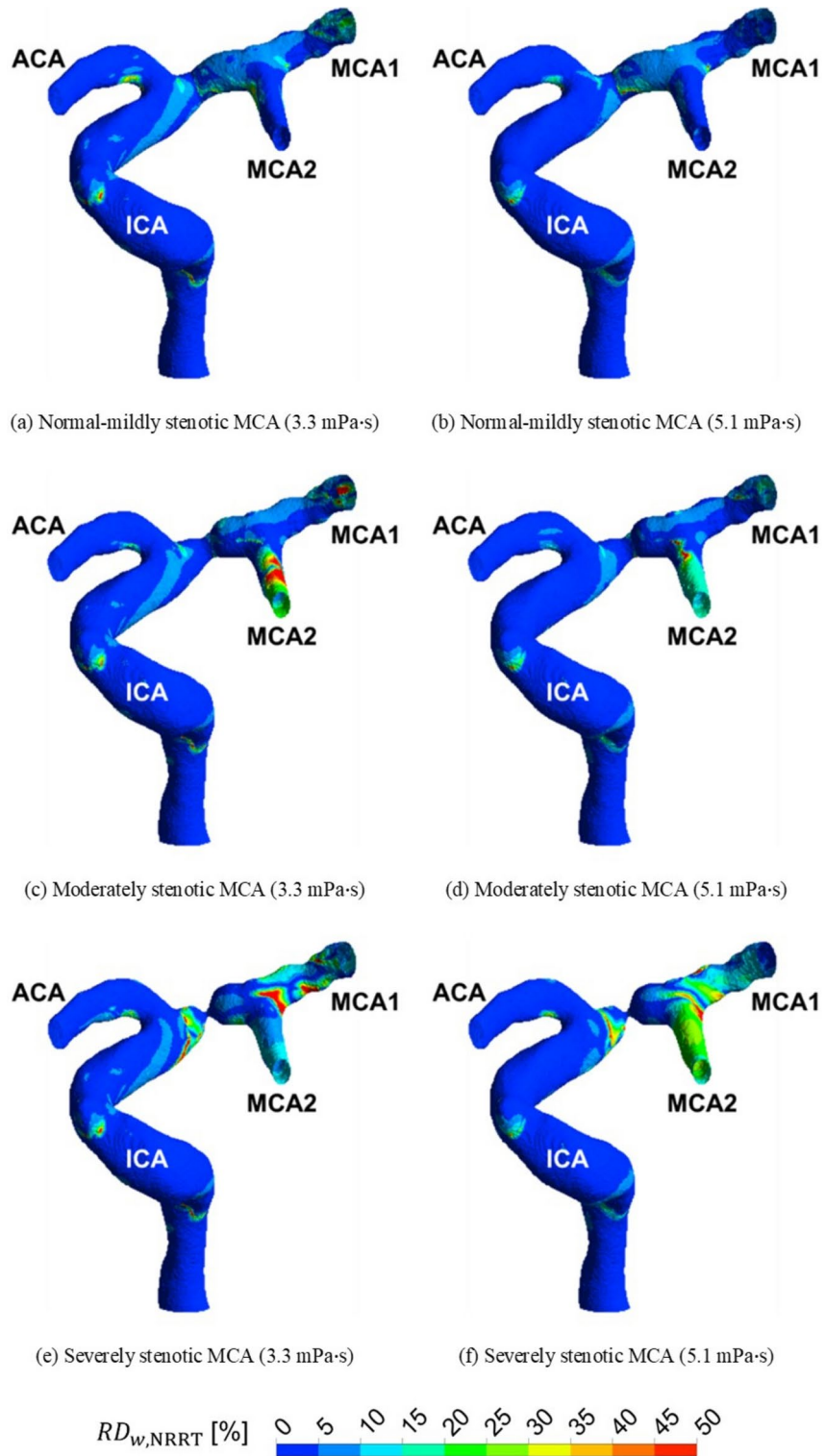


Fig. 14. Waveform-related relative difference contours of normalized relative residence time (NRRT).

over 20% higher than young adults at the ischemia location (MCA2 branch), indicating high risk of atheroma formation. Additionally, an inverse correlation was observed between the cycle-averaged WSS and OSI in the post-stenosis region along with the stenosis progression, which may cause further damage to the vascular walls.

With an increase in the blood viscosity, a decrease in FPR and an escalation in the maximum pressure gradient across the stenotic walls is expected due to the enhanced flow resistance. However, only a few studies investigated the influence of viscosity within authentic cerebrovascular networks. Through comprehensive and quantitative relative difference analysis, the study findings revealed that changes in viscosity slightly affected

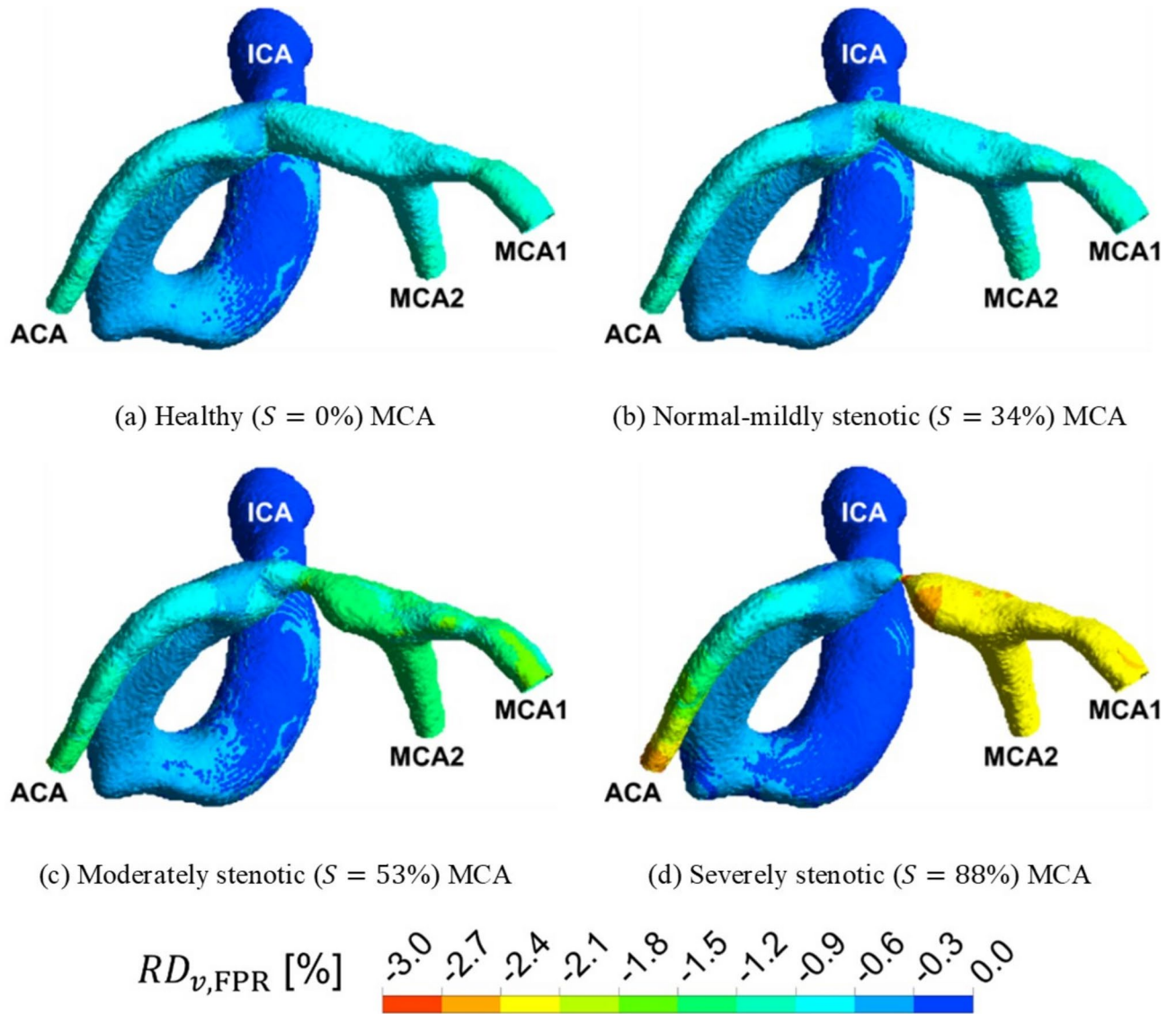


Fig. 15. Viscosity-related relative difference contours of fractional pressure ratio (FPR) (young adults, viscosity: 3.3→5.1 mPa·s).

both the maximum pressure gradient on stenotic walls and FPR, with variations remaining below 9% and 3%, respectively, despite a 54.5% increase in viscosity. These observations imply that an increase in viscosity scarcely contributes to plaque rupture risk inferred from flow-induced normal stress on stenotic walls. However, a decrease in the viscosity may promote the atherosclerotic plaque progression by enlarging the low shear zone.

The numerical analysis performed in this study presents quantitative hemodynamic insights of stenotic cerebral arteries encompassing various physiological factors, which help in obtaining a better understanding of the mechanisms of ischemic stroke. In future works, the impact of the stenosis shape such as the eccentricity or profile of the stenotic walls can be analyzed to obtain a better understanding of the cerebrovascular hemodynamics. Furthermore, the MAM proposed in this study can be further developed to simulate large-scale ROI by considering the phase lag.

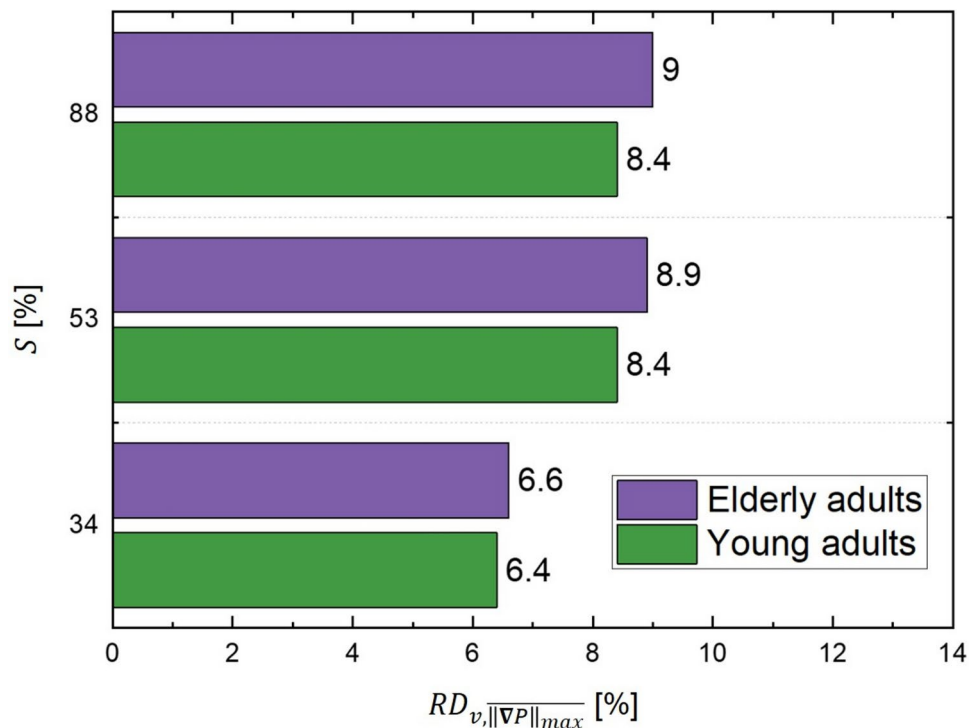


Fig. 16. Viscosity-related relative differences of cycle-averaged maximum pressure gradient magnitude (viscosity: 3.3 → 5.1 mPa-s).

Data availability

Data is provided within the manuscript or supplementary information files.

Received: 19 October 2024; Accepted: 14 February 2025

Published online: 03 April 2025

References

1. Tsao, C. W. et al. Heart disease and stroke statistics—2022 update: A report from the American Heart Association. *Circulation* **145**, e153–e639 (2022).
2. Kim, B. J. & Kim, J. S. Ischemic stroke subtype classification: An Asian viewpoint. *J. Stroke* **16**, 8–17 (2014).
3. Chandra, A., Stone, C. R., Li, W. A., Geng, X. & Ding, Y. The cerebral circulation and cerebrovascular disease II: Pathogenesis of cerebrovascular disease. *Brain Circ.* **3**, 57 (2017).
4. Tamargo, I. A., Baek, K. I., Kim, Y., Park, C. & Jo, H. Flow-induced reprogramming of endothelial cells in atherosclerosis. *Nat. Rev. Cardiol.* **20**, 738–753 (2023).
5. Brown, A. J. et al. Role of biomechanical forces in the natural history of coronary atherosclerosis. *Nat. Rev. Cardiol.* **13**, 210–220 (2016).
6. Kim, Y. S. et al. Distal versus proximal middle cerebral artery occlusion: Different mechanisms. *Cerebrovasc. Dis.* **47**, 238–244 (2019).
7. Ha, S. H. et al. Mechanism of stroke according to the severity and location of atherosclerotic middle cerebral artery disease. *J. Stroke Cerebrovasc. Dis.* **30**, 105503 (2021).
8. Hoi, Y. et al. Characterization of volumetric flow rate waveforms at the carotid bifurcations of older adults. *Physiol. Meas.* **31**, 291–302 (2010).
9. Jagoš, J. et al. In silico hemodynamical simulations show additional benefits of artery wall softening induced by antihypertensive drugs. *Comput. Methods Programs Biomed.* **245**, 108016 (2024).
10. Xu, L., Liang, F., Zhao, B., Wan, J. & Liu, H. Influence of aging-induced flow waveform variation on hemodynamics in aneurysms present at the internal carotid artery: A computational model-based study. *Comput. Biol. Med.* **101**, 51–60 (2018).
11. Yang, R. et al. Hematocrit and the incidence of stroke: A prospective, population-based cohort study. *Ther. Clin. Risk Manag.* **14**, 2081–2088 (2018).
12. Piemjaiswang, R., Ding, Y., Feng, Y., Piumsombon, P. & Chalermisinsuwan, B. Effect of transport parameters on atherosclerotic lesion growth: A parameter sensitivity analysis. *Comput. Methods Programs Biomed.* **199**, 105904 (2021).
13. Pijls, N. H. et al. Fractional flow reserve: A useful index to evaluate the influence of an epicardial coronary stenosis on myocardial blood flow. *Circulation* **92**, 3183–3193 (1995).
14. Liu, J. et al. Functional assessment of cerebral artery stenosis: A pilot study based on computational fluid dynamics. *J. Cereb. Blood Flow Metab.* **37**, 2567–2576 (2017).
15. De Bruyne, B. & Sarma, J. Fractional flow reserve: A review. *Heart* **94**, 949–959 (2008).
16. Liu, J. et al. Closed-loop geometric multi-scale heart-coronary artery model for the numerical calculation of fractional flow reserve. *Comput. Methods Programs Biomed.* **208**, 106266 (2021).
17. Pu, Y., Lan, L., Leng, X., Wong, L. K. & Liu, L. Intracranial atherosclerosis: From anatomy to pathophysiology. *Int. J. Stroke* **12**, 236–245 (2017).

18. Bit, A. et al. Three dimensional numerical analysis of hemodynamic of stenosed artery considering realistic outlet boundary conditions. *Comput. Methods Programs Biomed.* **185**, 105163 (2020).
19. Yoshikawa, Y. et al. On-site evaluation of CT-based fractional flow reserve using simple boundary conditions for computational fluid dynamics. *Int. J. Cardiovasc. Imaging* **36**, 337–346 (2020).
20. Zhang, Y., Furusawa, T., Sia, S. F., Umezu, M. & Qian, Y. Proposition of an outflow boundary approach for carotid artery stenosis CFD simulation. *Comput. Methods Biomech. Biomed. Engin.* **16**, 488–494 (2013).
21. Lo, S. C., McCullough, J. W. & Coveney, P. V. Parametric analysis of an efficient boundary condition to control outlet flow rates in large arterial networks. *Sci. Rep.* **12**, 19092 (2022).
22. Su, Z., Teng, W., Liu, Y., Wan, H. & Guo, Z. Hemodynamics study of anterior cerebral artery with different sac centerline lengths for rupture risk assessment. *Sci. Rep.* **14**, 22500 (2024).
23. Valipour, P. Effects of coiling embolism on blood hemodynamic of the MCA aneurysm: A numerical study. *Sci. Rep.* **12**, 22029 (2022).
24. Huang, C. et al. Analysis of the effects of stent-induced deformation on the hemodynamics of MCA aneurysms. *Sci. Rep.* **13**, 12356 (2023).
25. Gao, S., Lam, W. W., Chan, Y. L., Yan Liu, J. & Wong, K. S. Optimal values of flow velocity on transcranial Doppler in grading middle cerebral artery stenosis in comparison with magnetic resonance angiography. *J. Neuroimaging* **12**, 213–218 (2002).
26. Arzani, A. Accounting for residence-time in blood rheology models: Do we really need non-Newtonian blood flow modelling in large arteries?. *J. R. Soc. Interface* **15**, 20180486 (2018).
27. De Nisco, G. et al. Modelling blood flow in coronary arteries: Newtonian or shear-thinning non-Newtonian rheology?. *Comput. Methods Programs Biomed.* **242**, 107823 (2023).
28. Ameenuddin, M., Anand, M. & Massoudi, M. Effects of shear-dependent viscosity and hematocrit on blood flow. *Appl. Math. Comput.* **356**, 299–311 (2019).
29. Himburg, H. A. et al. Spatial comparison between wall shear stress measures and porcine arterial endothelial permeability. *Am. J. Physiol. Heart Circ. Physiol.* **286**, H1916–H1922 (2004).
30. Di Achille, P., Tellides, G., Figueroa, C. & Humphrey, J. A haemodynamic predictor of intraluminal thrombus formation in abdominal aortic aneurysms. *Proc. R. Soc. A.* **470**, 20140163 (2014).
31. Hoogendoorn, A. et al. Multidirectional wall shear stress promotes advanced coronary plaque development: Comparing five shear stress metrics. *Cardiovasc. Res.* **116**, 1136–1146 (2020).
32. Stamou, A. C., Radulovic, J. & Buick, J. M. Investigation of hemodynamic markers for stenosis development. *Eng. Rep.* **3**, e12389 (2021).
33. Gallo, D. et al. Segment-specific associations between local haemodynamic and imaging markers of early atherosclerosis at the carotid artery: An in vivo human study. *J. R. Soc. Interface* **15**, 20180352 (2018).
34. Timmins, L. H. et al. Oscillatory wall shear stress is a dominant flow characteristic affecting lesion progression patterns and plaque vulnerability in patients with coronary artery disease. *J. R. Soc. Interface* **14**, 20160972 (2017).
35. John, L., Pustějovská, P. & Steinbach, O. On the influence of the wall shear stress vector form on hemodynamic indicators. *Comput. Visual. Sci.* **18**, 113–122 (2017).
36. He, X. & Ku, D. N. Pulsatile flow in the human left coronary artery bifurcation: Average conditions. *J. Biomech. Eng.* **118**, 74–82 (1996).
37. Ford, M. D., Alperin, N., Lee, S. H., Holdsworth, D. W. & Steinman, D. A. Characterization of volumetric flow rate waveforms in the normal internal carotid and vertebral arteries. *Physiol. Meas.* **26**, 477–488 (2005).
38. Chnafa, C., Brina, O., Pereira, V. & Steinman, D. Better than nothing: A rational approach for minimizing the impact of outflow strategy on cerebrovascular simulations. *AJNR Am. J. Neuroradiol.* **39**, 337–343 (2018).
39. Luisi, C. A. et al. Evaluating the accuracy of cerebrovascular computational fluid dynamics modeling through time-resolved experimental validation. *Sci. Rep.* **14**, 8194 (2024).
40. Shi, Y., Lawford, P. & Hose, R. Review of zero-D and 1-D models of blood flow in the cardiovascular system. *Biomed. Eng. OnLine* **10**, 1–38 (2011).
41. Westerhof, N., Lankhaar, J.-W. & Westerhof, B. E. The arterial Windkessel. *Med. Biol. Eng. Comput.* **47**, 131–141 (2009).
42. Dubs, L. et al. Assessment of extracranial carotid artery disease using digital twins—A pilot study. *NeuroImage Clin.* **38**, 103435 (2023).
43. Zarrinkoob, L. et al. Blood flow distribution in cerebral arteries. *J. Cereb. Blood Flow Metab.* **35**, 648–654 (2015).
44. Seymour, R. S., Hu, Q. & Snelling, E. P. Blood flow rate and wall shear stress in seven major cephalic arteries of humans. *J. Anat.* **236**, 522–530 (2020).
45. Li, X. et al. Numerical simulation of haemodynamics and low-density lipoprotein transport in the rabbit aorta and their correlation with atherosclerotic plaque thickness. *J. R. Soc. Interface* **14**, 20170140 (2017).
46. Mpairaktaris, D. G., Soulis, J. V. & Giannoglou, G. D. Low density lipoprotein transport through patient-specific thoracic arterial wall. *Comput. Biol. Med.* **89**, 115–126 (2017).
47. Wang, H., Balzani, D., Vedula, V., Uhlmann, K. & Varnik, F. On the potential self-amplification of aneurysms due to tissue degradation and blood flow revealed from FSI simulations. *Front. Physiol.* **12**, 785780 (2021).
48. Li, Z.-Y. et al. The mechanical triggers of plaque rupture: Shear stress vs pressure gradient. *Br. J. Rad.* **82**, S39–S45 (2009).
49. Soulat, G., McCarthy, P. & Markl, M. 4D flow with MRI. *Annu. Rev. Biomed. Eng.* **22**, 103–126 (2020).
50. Granata, A. et al. Doppler ultrasound and renal artery stenosis: An overview. *J. Ultrasound* **12**, 133–143 (2009).
51. Kang, T., Mukherjee, D. & Ryu, J. Numerical investigation of carotid stenosis in three-dimensional aortic-cerebral vasculature: Pulsatility index, resistive index, time to peak velocity, and flow characteristics. *Eng. Appl. Comput. Fluid Mech.* **15**, 1645–1665 (2021).
52. Sun, H. T., Sze, K. Y., Chow, K. W. & On Tsang, A. C. A comparative study on computational fluid dynamic, fluid-structure interaction and static structural analyses of cerebral aneurysm. *Eng. Appl. Comput. Fluid Mech.* **16**, 262–278 (2022).

Acknowledgements

This work was supported by the National Research Foundation of Korea (NRF) grant funded by the Korean Government (MSIT) [No. 2020R1A2C2100077]. This work was also supported by the Institute for Korea Spent Nuclear Fuel (iKSNF) and Korea Foundation of Nuclear Safety (KOFONS) grant funded by the Korean Government (Nuclear Safety and Security Commission, NSSC) [No. RS-2021-KN066120]. The authors thank ANSYS Korea for its invaluable support and donations.

Author contributions

J.C.: Conceptualization, Methodology, Software, Validation, Formal analysis, Investigation, Data curation, Visualization, Writing—Original Draft, Writing—Review & Editing. M.C.: Data curation, Writing—Review & Editing. S.S.: Formal analysis, Writing—Review & Editing. J.K.: Investigation, Writing—Review & Editing. H.K.: Resources, Writing—Review & Editing. B.K.: Project administration, Funding acquisition, Writing—Review &

Editing. H.J.: Conceptualization, Resources, Supervision, Project administration, Funding acquisition, Writing—Review & Editing.

Declarations

Competing interests

The authors declare no competing interests.

Additional information

Supplementary Information The online version contains supplementary material available at <https://doi.org/10.1038/s41598-025-90604-0>.

Correspondence and requests for materials should be addressed to H.J.

Reprints and permissions information is available at www.nature.com/reprints.

Publisher's note Springer Nature remains neutral with regard to jurisdictional claims in published maps and institutional affiliations.

Open Access This article is licensed under a Creative Commons Attribution-NonCommercial-NoDerivatives 4.0 International License, which permits any non-commercial use, sharing, distribution and reproduction in any medium or format, as long as you give appropriate credit to the original author(s) and the source, provide a link to the Creative Commons licence, and indicate if you modified the licensed material. You do not have permission under this licence to share adapted material derived from this article or parts of it. The images or other third party material in this article are included in the article's Creative Commons licence, unless indicated otherwise in a credit line to the material. If material is not included in the article's Creative Commons licence and your intended use is not permitted by statutory regulation or exceeds the permitted use, you will need to obtain permission directly from the copyright holder. To view a copy of this licence, visit <http://creativecommons.org/licenses/by-nc-nd/4.0/>.

© The Author(s) 2025